

UDC 533.6.011.55 :
536.2

**TECHNICAL REPORT OF NATIONAL
AEROSPACE LABORATORY**

TR-494T

**Study on Lee-Surface Heating over Yawed
Blunt Cone in Hypersonic Flow**

Shigeaki NOMURA

March 1977

NATIONAL AEROSPACE LABORATORY

CHŌFU, TOKYO, JAPAN

Study on Lee-Surface Heating over Yawed Blunt Cone in Hypersonic Flow*

By Shigeaki NOMURA**

ABSTRACT

Theoretical and experimental studies have been conducted on three-dimensional laminar heat transfer over a blunt cone, at moderate angles of attack, in a hypersonic flow of Mach number 7. With the exception of lee-surface heating in a separated region, the small cross flow theory together with three-dimensional inviscid flow solutions was found to agree quite well with the experimental data. From the comparison between experimental results and three-dimensional inviscid flow solutions, it was found that the interaction effect of the separated boundary layer over the lee-surface was small. With regard to heat transfer distribution on the lee-meridian plane, a new concept of cross flow energy thickness has been drawn from the energy integral of the three-dimensional boundary layer equations. From this concept, it has been exhibited analytically that once the cross flow separation occurs, heat transfer increases significantly along the most leeward generator due to negative cross flow displacement thickness. The correlation equation for heat transfer along the most leeward generator has been introduced from similar solutions of boundary layer equations and has been found to agree quite well with the experimental data on several different conditions.

概 要

極超音速流中に、半頂角程度の迎角をもって置かれた、鈍頭円錐への層流熱伝達に関する理論的、実験的研究を行った。先ず、物体周りの三次元非粘性流の数値解を求め、これを三次元境界層の微小横断流近似による熱伝達相関式の境界条件として適用した。その結果、風上および側面領域では、熱伝達の実験値と良く一致するが、剝離を含む風下領域では、実験値が顕著に増加し、近似解とは大幅にずれる事を示した。次に、表面圧力、熱伝達およびオイルフロウの実験結果の検討、ならびに非粘性解との比較から、この迎角範囲では、剝離領域においても、粘性非粘性流の相互干渉は弱く、境界層理論が適用可能な事を示した。風下対称面で、三次元境界層方程式のエネルギー積分を求めて、新たに横断流エネルギー厚さの定義を与え、これによって風下側での熱伝達の増加は、剝離による境界層排除厚さの減少の結果生ずる事を定性的に明らかにした。更に、風下対称面上の境界層に放物型相似則を仮定し、境界層方程式の数値解を求め、その境界層端での条件をパラメータとした熱伝達相関式を与えた。この相関式を用いて、風下対称面上での熱伝達を求め、実験値との良い一致を得た。

TABLE OF CONTENTS

CHAPTER	Page
ABSTRACT	1
TABLE OF CONTENTS	1
NOMENCLATURE	2
I INTRODUCTION	3
II EXPERIMENTAL INVESTIGATIONS	5
2.1 Test Facilities and Model Configurations	
2.2 Experimental Results	5
III NUMERICAL ANALYSIS OF	6

THREE-DIMENSIONAL INVISCID FLOW

3.1 Method of Numerical Analysis	10
3.1.1 Review of Numerical Methods	10
3.1.2 3-D Steady Eulerian Equations	11
3.2 Inviscid Flow Solutions	13
3.2.1 Shock Wave and Shock Layer	13
3.2.2 Surface Pressure and Streamlines	16
IV THEORETICAL ANALYSIS OF THREE-DIMENSIONAL BOUNDARY LAYER AND HEAT TRANSFER	18
4.1 Basic Equations	18
4.2 Small Cross Flow Approximation	18

* Received March 2, 1977.

** First Aerodynamics Division.

4.2.1 Axisymmetric Analogy	18
4.2.2 Heat Transfer Solutions	19
4.3 Three-Dimensional Analysis along Most Leeward Generator	20
4.3.1 Similar Transformation	20
4.3.2 Energy Integral Equation	21
4.3.3 Locally Similar Solutions at $y=0$	23
V CONCLUSIONS	26
ACKNOWLEDGEMENTS	26
REFERENCES	26
APPENDIX A	28
APPENDIX B	29
APPENDIX C	29

NOMENCLATURE

$[A],[B],[C],[D]$: coefficient matrix defined in APPENDIX A
 $[AF^n][AQ^n][AG^n]$: coefficient matrix defined in APPENDIX C
 a : speed of sound
 a : Fourier coefficients
 b_1 : $\left(\frac{\rho_\infty}{\rho}-1\right)\left(u_{1\infty}-\frac{u_{2\infty}}{r_s}\frac{\partial r_s}{\partial \phi}-u_{3\infty}\frac{\partial r_s}{\partial z}\right)\frac{1}{\pi_s}$
 b_2 : $(\tilde{V}\cdot\tilde{n}_{wall})_{i+1,j,k}$
 b_3 : $\left[\left(\tilde{u}_1-\frac{b_2}{b}\right)^2+\left(\tilde{u}_2+\frac{1}{r_b}\frac{\partial r_b}{\partial \phi}\frac{b_2}{\kappa_b}\right)^2+\left(\tilde{u}_3+\frac{\partial r_b}{\partial z}\frac{b_2}{\kappa_b}\right)^2\right]^{1/2}$
 C : $\rho\mu/(\rho\mu)_w$
 \hat{C} : C/Pr
 c_p : specific heat or $(p-p_\infty)/(\rho_\infty V_\infty^2/2)$
 d : diameter of spherical nose
 \bar{E} : row vector defined in eq. (3-5)
 f : $\int \frac{u}{u_e} d\eta$ or function in eq. (3-4)
 $F1$: $\frac{\partial f}{\partial \eta}$
 $[G]$: amplification matrix
 g : H/H_e or function in eq. (3-4)
 G_e : h_e/H_e
 H : $h+(u^2+v^2)/2$
 \bar{H} : row vector in eq. (3-5)
 h : $c_p T$
 h_1, h_2, h_3 : metric coefficients of x_1, x_2, x_3
 \bar{h}_1 : $\Delta X/\Delta Z$
 \bar{h}_2 : $\Delta Y/\Delta Z$
 (i,j,k) : finite difference mesh coordinates
 $[I]$: unit matrix
 k : thermal conductivity coefficient of air

M : Mach number
 M_ϕ : Mach number of ϕ velocity component
 m : source strength of out flow
 p : pressure
 Pr : Prandtl number
 Q : $\int \frac{v}{u_e} d\eta$
 $Q1$: $Q\eta$
 \dot{q}_w : heat transfer rate to the wall
 Rn : spherical nose radius
 (r,ϕ,z) : cylindrical coordinate system
 r_b : r coordinate of the body surface
 r_s : r coordinate of shock wave
 S : entropy
 s : length measured along cone generator
 T : temperature
 u_1, u_2, u_3 : velocity components in r, ϕ, z directions
 u, v, w : velocity components in x_1, x_2, x_3
 V : magnitude of velocity vector
 X, Y, Z : transformed coordinate in eq. (3-4)
 $\Delta X, \Delta Y, \Delta Z$: mesh size in X, Y, Z coordinates
 x : length measured along inviscid surface streamline
 x_1 : coordinate along the streamline in the streamline coordinate system
 x_2 : coordinate normal to x_1 and tangent to the wall
 x_3 : length measured normal to the wall
 y : x_2 coordinate along the most leeward generator
 z : length measured along cone axis from the top of the model
 α : angle of attack
 $\beta_i; i=1\sim 4$: boundary layer parameters defined in eq. (4-25)
 $\hat{\beta}_1, \hat{\beta}_2$: β_1/G_e and β_2/G_e respectively
 β : $\sqrt{M^2-1}$
 γ : ratio of specific heats
 δ^* : displacement thickness of boundary layer
 δ_f^* : streamwise δ^* in eq. (4-33)
 δ_Q^* : cross flow δ^* in eq. (4-33)
 η : transformed coordinate in eq. (4-20)
 $\bar{\eta}$: $u_3^2-a^2$
 θ : energy thickness
 θ_f : streamwise θ in eq. (4-29)
 θ_Q : cross flow θ in eq. (4-29)
 θ_c : half cone angle
 κ_c : $\sqrt{1+\left(\frac{1}{r_b}\frac{\partial r_b}{\partial \phi}\right)^2+\left(\frac{\partial r_b}{\partial z}\right)^2}$

- κ_z : lateral curvature in inviscid streamline of $\frac{1}{h_1 h_2} \frac{\partial h_1}{\partial x^2}$
- κ_s : $\sqrt{1 + \left(\frac{1}{r_s} \frac{\partial r_s}{\partial \phi}\right)^2 + \left(\frac{\partial r_s}{\partial z}\right)^2}$
- $\lambda_{Cm}, \lambda_{Dm}$: a larger value in $\lambda_{Cs}, \lambda_{Ds}$, respectively
- λ_C, λ_D : eigenvalue of matrices $[C], [D]$, respectively
- ξ : transformed coordinate in eq. (4-20)
- ρ : density
- τ : shear force
- ϕ : circumferential angle
- $\hat{\phi}$: $\pi - \phi$
- ψ : function defined in eq. (4-21)
- ω : $\sqrt{-1}$
- μ : viscosity
- subscripts
- i, j, k : value estimated at (i, j, k)
- i : value at the sphere-cone junction
- p : component normal to trough of isobaric line
- n : normal component
- o, st : stagnation point value
- $w, wall$: value at the wall
- ∞ : free stream condition
- superscripts
- n : iteration number
- (\sim) : value at predictor stage

I. INTRODUCTION

Though the study of three-dimensional flow has a long history¹¹⁻¹³, detailed and extensive investigations of this field have been made recently in connection with the actual requirements from the hypersonic flight and lifting re-entry program. Among several unknown problems remained in this field¹⁴ with an actual importance, the heat transfer problem accompanied by a three-dimensional flow separation over a blunt body at a high angle of attack has attracted a number of investigations: experiments about a severe heating on the upper surface of a vehicle⁵⁻⁷, fundamental experiments for lifting body⁸⁻¹⁰, experiments about flow separation¹¹⁻¹⁵ and numerous theoretical and numerical investigations¹⁶⁻³⁴.

For the purpose of physical understanding of a separated flow in three-dimensions, Tracy³⁵ was the first to measure a detailed profiles of static and pitot pressure distributions and head transfer over a surface of yawed sharp cone in a hypersonic flow of Mach number 7.95.

Tracy showed a thick separated viscous layer, an embedded cross flow shock wave over a leeward surface, and peaks of surface pressure and heat transfer at the leeward meridian plane.

The leeward phenomena became more clear from the experiments by Whitehead et al.^{36, 37} and Stetson³⁸. Whitehead et al. visualized a viscous flow over a leesurface of a delta wing at an angle of attack by a flow visualization technique³⁹ in a hypersonic flow of Mach number 6. They observed a small pair of vortices, the thinning of boundary layer between vortices, and the remarkable heat transfer increase along the centerline. They explained this heat transfer increase by mixing and thinning of boundary layer caused by a pair of vortices.

Stetson measured surface and pitot pressure distributions in detail over sharp and blunt cones at angles of attack in a hypersonic flow of Mach number 14.2. From these data, Stetson presented a separated flow model with a pair of vortices named "Stream Ribbons" over the leeward surface.

Regarding to the three-dimensional flow separation, Maskell³⁸ proposed two typical patterns; a bubble type structure with an isolated singular point and a free vortex layer type structure without any singularity. The separated flow models with a pair of vortices proposed by Whitehead et al. and Stetson belong to a free vortex layer type classified by Maskell. However, Maskell did not show a detailed flow properties of a separated flow.

On the otherhand, the theoretical and numerical investigations of the three-dimensional flow have been conducted actively in this decade. The methods of theoretical approaches to the three-dimensional viscous flow can be classified into three categories; (1) boundary layer analysis with a small cross flow approximation (2) three-dimensional boundary layer analysis restricted on a symmetric plane of a yawed body (3) complete numerical solution of the fully three-dimensional viscous flow.

Due to the axisymmetric analogy introduced by assuming a small cross flow in three-dimensional boundary layer equations, the heat transfer distribution can be calculated by the well established correlation equation in two-dimensional flow. Vaglio-Laurin⁴⁰ showed the applicability of the small cross flow approximation even along a highly curved inviscid surface streamline around a stagnation region

of a blunted body in a hypersonic flow. In order to apply the small cross flow method, the geometry of inviscid surface streamlines and flow properties along them should be determined in advance where the numerical procedures for them become very complicated in three-dimensional flow. DeJarnette¹⁹⁾ provided a simplified method for these procedures by using Newtonian flow and showed good results for heat transfer over a three-dimensional body. However, this method is, of course, not applicable for a separated flow due to a severe cross flow in it.

As shown by Raetz's dependence-influence principle²⁾, the flow along a symmetry plane of a yawed body can be determined independently of the flow outside of this plane. The three-dimensional boundary layer analysis on a leeward symmetric plane was done first by Moore⁴¹⁾ about a sharp cone at angles of attack with an assumption of parabolic similarity of Blasius type. He, however, could obtain solutions only for a small angle of attack without separation. Libby et al.⁵⁸⁾ solved compressible boundary layer equations with a parabolic similarity assumption at a hypersonic speed where they emphasized the importance only of a streamwise pressure gradient as in a two-dimensional case. The successful treatment on a symmetric plane was done by Wang^{26), 27)} about incompressible flow on a spheroid at angles of attack in subsonic flow without similarity assumption. From the numerical solutions, Wang showed possible separation patterns of a free vortex layer type and a bubble type over a lee-surface of spheroid.

In regard to the numerical solutions of three-dimensional boundary layer equations over a blunt cone at an angle of attack, Der⁸¹⁾ and Fannelop¹⁹⁾ could not obtain a separated flow reasonably. Der suggested a bubble type separation with a singular point on a lee-surface and Fannelop could not obtain any separation; both results do not agree with experiments. However, Fannelop pointed out interesting remarks that the heat transfer result given by a parabolic similarity assumption agreed quite well with the nonsimilar solutions over the leeward region with strong cross flow, even though the detailed flow profiles across the boundary layer were affected significantly by nonsimilar effects.

More recently, the flow with cross flow separation has been solved successfully over a sharp cone at angles of attack by Lin and Rubin²⁰⁾, Lubard and Helliwell²¹⁾ and McRae²⁴⁾.

Lin and Rubin used experimental pressure data for the computation of the three-dimensional boundary layer equations where they remained second derivative terms of velocity with respect to ϕ to avoid numerical instability at the cross flow separation. The solutions show a pair of vortices and heat transfer peak on a leeward meridian. The methods of Lubard and Helliwell and McRae are the numerical solutions of Navier-Stokes equations with assumptions of negligible streamwise derivatives in viscous terms and of the complete conical flow, respectively. The former obtained a pair of vortices and a heat transfer peak in ϕ direction, and the later obtained a pair of vortices and a vortical singularity lifted off the lee-surface at large angles of attack. In these analysis, Lin and Rubin pointed out important flow behaviors on a leeward meridian plane as follows; (1) for $\alpha \ll \theta_c$, flow shows parabolically similar behavior (2) for $\alpha < \theta_c$, the detailed flow profiles across the boundary layer do not have similarity due to a thick mass flow accumulation, but a heat transfer distribution has a parabolic similar profile (3) for $\alpha \geq \theta_c$, a thick layer moves out of the symmetric plane and flow again becomes to have similar profiles.

Though Moore⁴¹⁾ suggested a parabolic similarity for a case of conical external flow, the item (2) in Lin and Rubin shows nonsimilar flow and this thick nonsimilar boundary layer may give the nonuniqueness in similar solution of Moore. This item (2) is the same as the result pointed out by Fannelop¹⁹⁾.

In addition to these viscous flow studies, a number of numerical investigations about the three-dimensional inviscid flow have been conducted which are essential for the boundary layer analysis. A brief review of these studies is to be presented in chapter III of this paper.

Although several experiments and numerical solutions have provided fairly clear-cut flow models and fairly good numerical predictions, the physical causality and mechanism of the heat transfer increase in a separated flow have not become clear yet. Main reason for this unclearness, seems to the author, will be in consequence of the complete numerical treatment in the theoretical investigations and, therefore, this situation will require analytical and semi-empirical investigations for this problem.

In this paper, under these circumstances, theoretical and experimental investigations have been conducted about heat transfer over

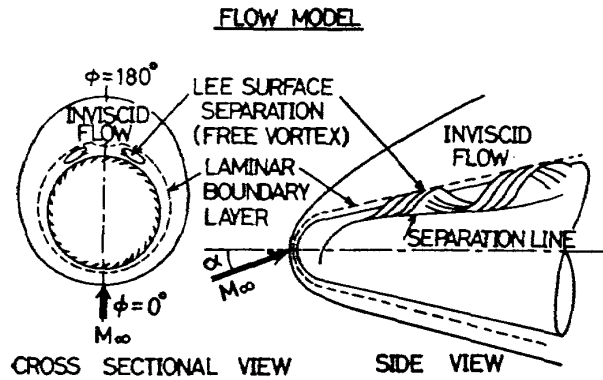


Fig. 1. Flow Model

a blunt cone at angles of attack in a hypersonic flow.

In chapter II, experimental apparatus, test facilities, and experimental results are presented. The purpose of this experiments is to obtain physical features of flow in order to provide useful informations for a theoretical treatment of it. The experimental results have suggested a separable treatment of inviscid flow and laminar boundary layer flow as shown in the flow model of Fig. 1. Then, the three-dimensional Eulerian equations have been solved numerically in chapter III. There are presented a short review of numerical methods, a brief explanation for the applied method, and the numerical solutions compared with experimental results. The purposes of this numerical computation are to estimate the order of viscous interaction effect and secondary flow in a boundary layer, and to obtain the inviscid flow structure, the inviscid flow geometry on the surface and inviscid flow conditions on the outer edge of the boundary layer. In chapter IV, analyses of three-dimensional boundary layer are described. The semi-empirical method with small cross flow approximation has been applied first. The main purpose of this chapter is to provide an analytical explanation and the quantitative correlation equation for heat transfer in a separated region along the most leeward generator.

For computation of Eulerian equations and boundary layer equations, the 2 CPU System of FACOM 230-75 electric computers was employed.

II. EXPERIMENTAL INVESTIGATIONS

The detailed measurements of surface pressure, heat transfer and limiting streamlines over a blunt cone at angles of attack have been

conducted in a hypersonic flow of nominal Mach number 7.

In this chapter, a brief explanation of experimental apparatus and the detailed investigations about experimental results are presented.

2.1. Test Facilities and Model Configuration

Tests have been done using 50 cm ϕ hypersonic wind tunnel in National Aerospace Laboratory of Japan: the main characteristics of the wind tunnel are listed in Table 1. A model supporting system is of gimbals-strut type and its angle of attack can be changed by $\pm 20^\circ$ during a run. A model can be shot into a flow at any time with a travelling time of less than 1 sec.

The model configurations (Fig. 2) are as follows; an interchangeable spherical nose with $Rn=5, 10, 15$ mm, the half cone angle $\theta_c=15^\circ$ and the axial length for $Rn=10$ mm of 264.3 mm.

The pressure model has 43 surface pressure holes with 1 mm ϕ over a half cone surface along generators of $\phi=0^\circ, 45^\circ, 90^\circ, 135^\circ, 157.5^\circ$ and 180° . Two sets of pressure transducers of variable reluctance type with scanning valves were set inside of a sting close to the model base.

Table 1. NAL Hypersonic Wind Tunnel

Type	Blow Down
Test Section	Free Jet, 50 cm ϕ
Nozzle	Axisymmetric, Contour
Heater	Pebble Bed of Alumina
Po	10-100 ata
To	300-1000°C
Duration	30-200 sec
Mach number	5, 7, 9, 11

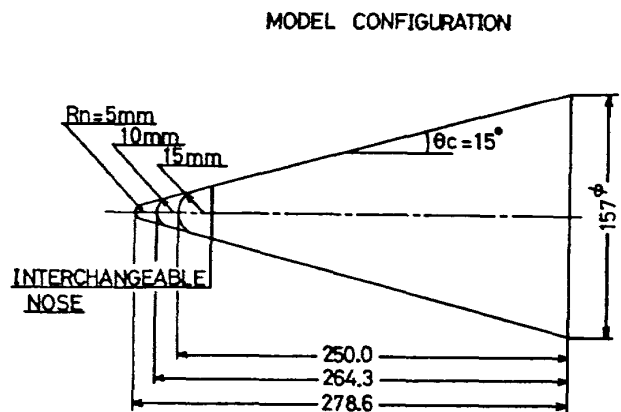


Fig. 2. Model Configuration

The heat transfer model has 32 probes installed over a half cone surface along generators of $\phi=0^\circ-180^\circ$ at 30° interval. The probe is made of a small copper slug sensor thermally shielded by ceramics, and the transient temperature rise of the sensor is measured by thermo-couple to determine heat transfer rate. The heat transfer model was shot into a flow after the total temperature of a flow had become stable.

The oil flow model has 72 holes of oil exits with $0.5\text{mm}\phi$ from which vacuum pump oil colored by lump black is pushed out slowly. The oil moved by shear force drew clear streaks which showed limiting streamlines over a surface. Pictures of oil streaks were taken during a run from windward, sideward and leeward directions.

2.2. Experimental Results

Fig. 3a shows a schlieren photograph taken from the sideward of a blunt cone with $Rn=15\text{ mm}$ at an angle of attack $\alpha=15^\circ$ in $M_\infty=7.1$.

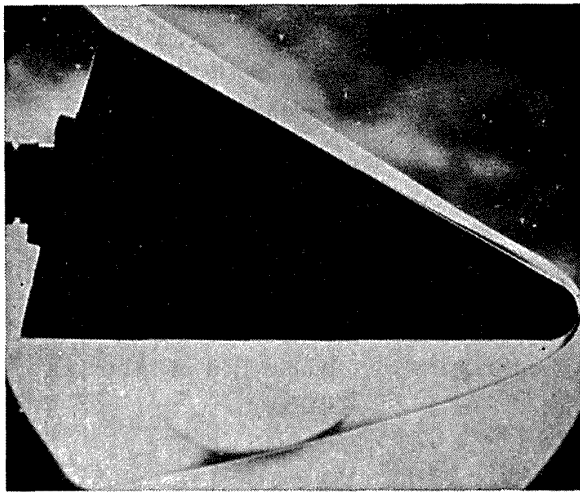


Fig. 3a. Schlieren Picture ($\alpha=15^\circ$, $M_\infty=7.1$)

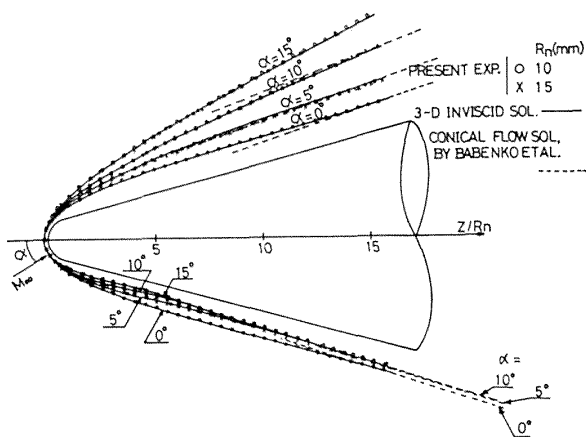


Fig. 3b. Shock Wave Patterns

As seen in the windward region, the photograph shows clearly an adversely curved shock wave and compression waves caused by an overexpansion-recompression process after the curvature discontinuity at the sphere-cone junction. However, density is too small to see a viscous layer in the leeward region.

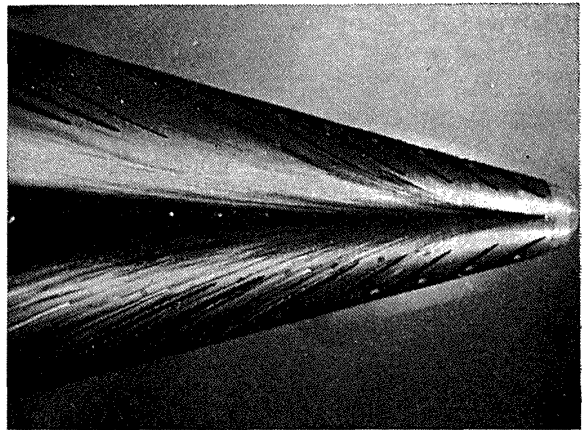


Fig. 4a. Oil Flow Visualization; $\alpha=15^\circ$ $\phi=0^\circ$, $Rn=15\text{ mm}$

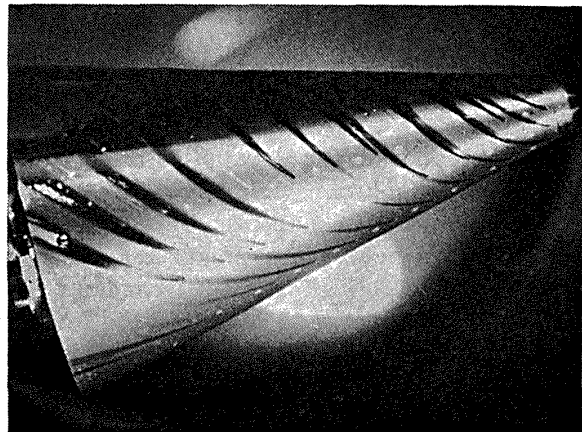


Fig. 4b. Oil Flow Visualization; $\alpha=15^\circ$, $\phi=90^\circ$, $Rn=15\text{ mm}$

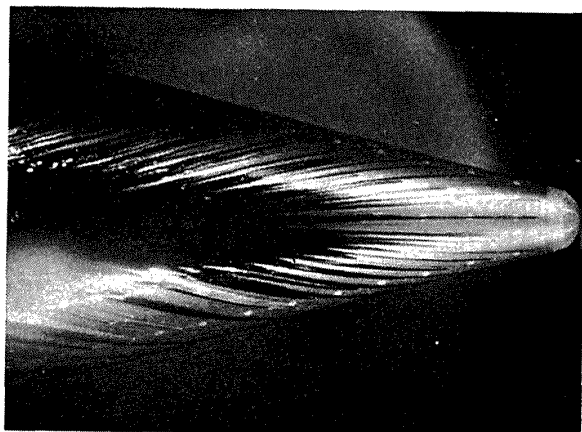


Fig. 4c. Oil Flow Visualization; $\alpha=5^\circ$, $\phi=180^\circ$, $Rn=15\text{ mm}$

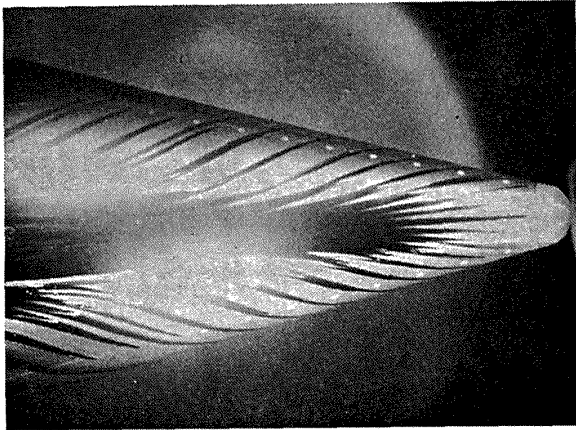


Fig. 4d. Oil Flow Visualization; $\alpha=10^\circ$, $\phi=180^\circ$, $Rn=15$ mm

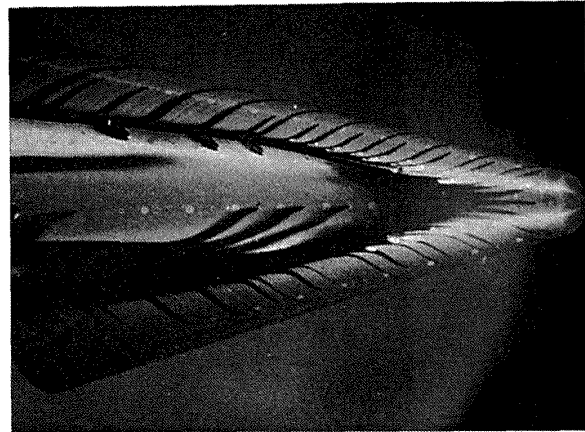


Fig. 4g. Oil Flow Visualization; $\alpha=20^\circ$, $\phi=180^\circ$, $Rn=15$ mm

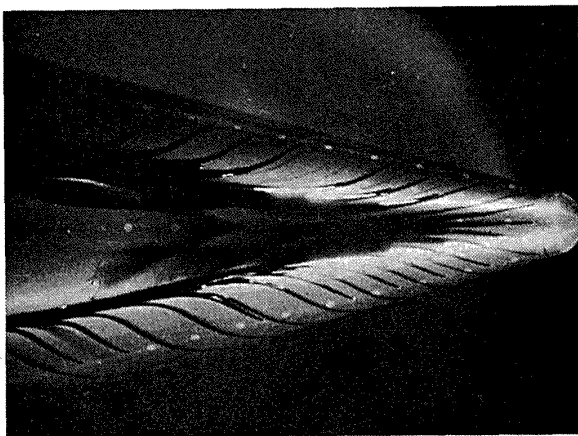


Fig. 4e. Oil Flow Visualization; $\alpha=15^\circ$, $\phi=180^\circ$, $Rn=15$ mm

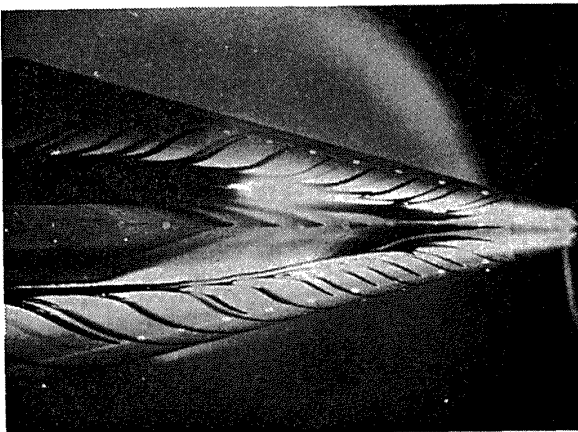


Fig. 4f. Oil Flow Visualization; $\alpha=15^\circ$, $\phi=180^\circ$, $Rn=10$ mm

In Figs. 4, pictures of oil flow visualization are shown which were taken from the three different directions for the conditions of $\alpha=5^\circ$, 10° , 15° , and 20° with $Rn=10$ mm and 15 mm in $M_\infty=7.1$ during each run. The pictures taken from windward and sideward directions show a strong cross flow rolling up from the stagnationline of $\phi=0^\circ$ to the leeward region.

The pictures of the leeward side show only an oil accumulation at $\alpha=5^\circ$, a very small region of separation at $\alpha=10^\circ$, a widely separated region at $\alpha=15^\circ$, and a strong reverse cross flow in a widely separated region at $\alpha=20^\circ$. Since the half cone angle θ_c is 15° , the result at $\alpha=10^\circ$ shows that the separation can occur on the surface with a positive local angle of attack. Comparing the photographs for $Rn=10$ and 15 mm at $\alpha=15^\circ$ (Figs. 4e, 4f), oil streaks and patterns of separated regions of

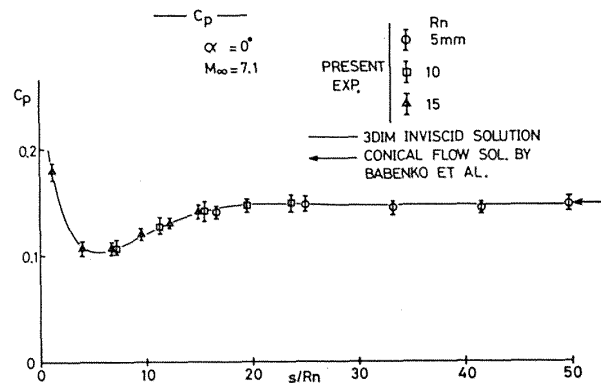


Fig. 5a. Longitudinal Pressure; $\alpha=0^\circ$

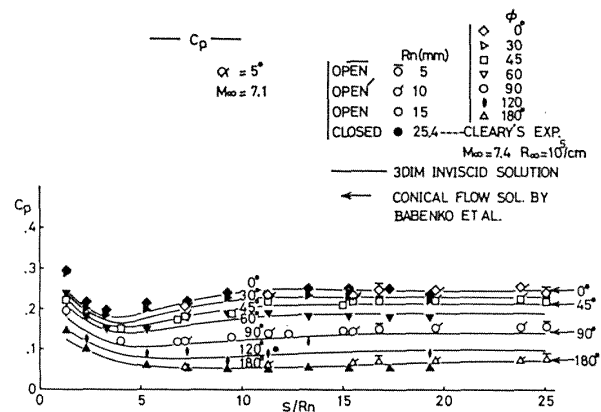
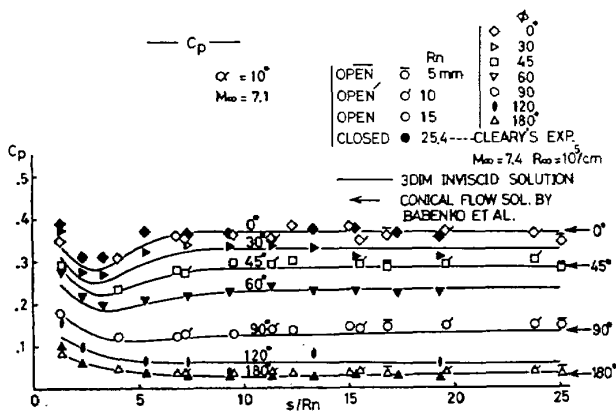
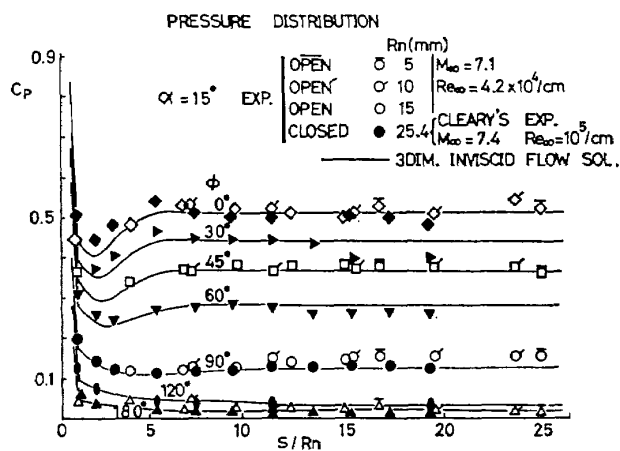
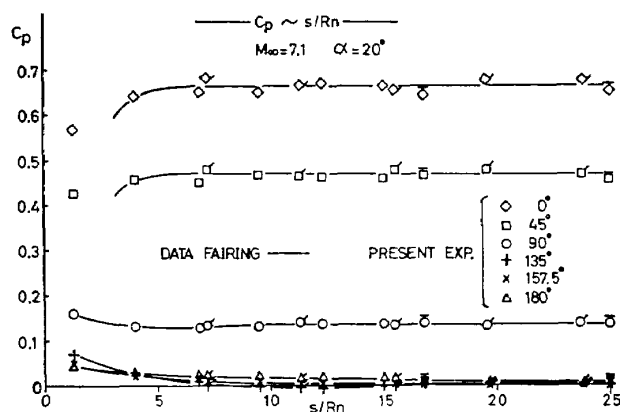
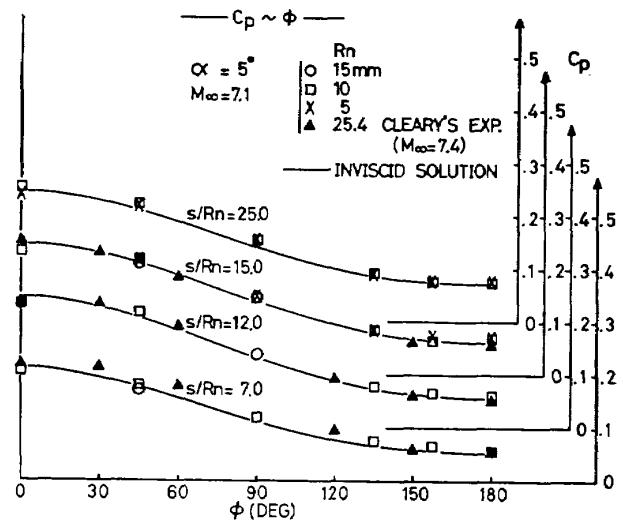
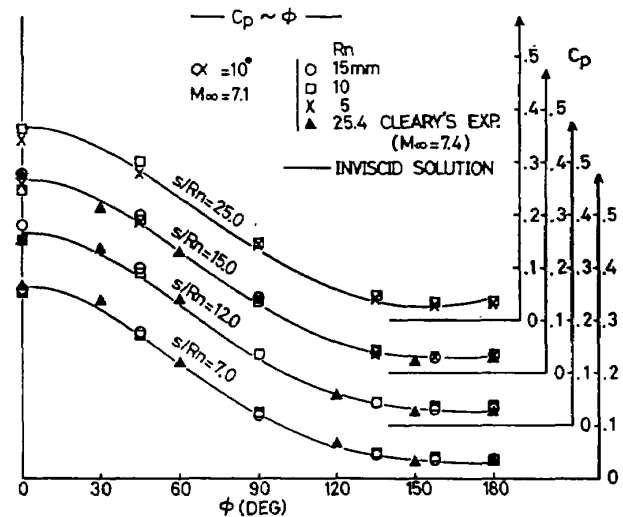
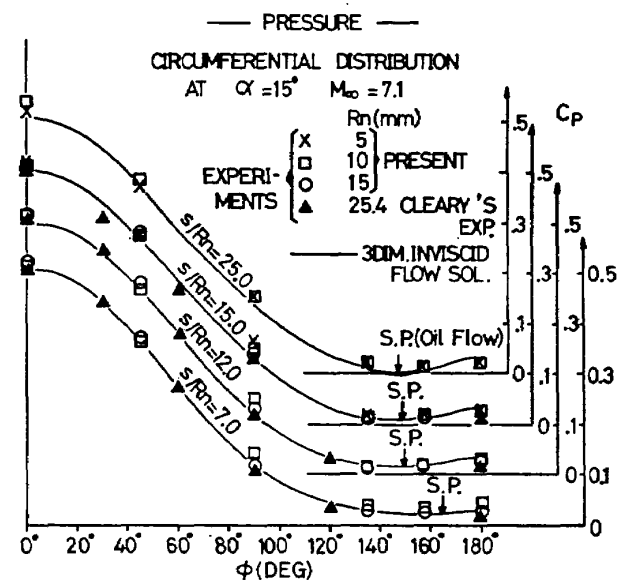


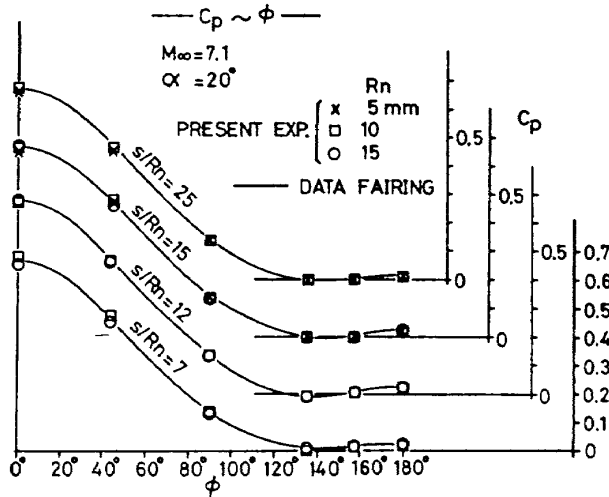
Fig. 5b. Longitudinal Pressure; $\alpha=5^\circ$

Fig. 5c. Longitudinal Pressure; $\alpha = 10^\circ$ Fig. 5d. Longitudinal Pressure; $\alpha = 15^\circ$ Fig. 5e. Longitudinal Pressure; $\alpha = 20^\circ$

both cases become duplicate completely, if the surface length of the cone is normalized by R_n in the pictures.

In Fig. 5, pressure distributions for $R_n = 5$, 10, and 15 mm are shown against length s measured along each generator from the top of the model in a normalized form by R_n . Also in Fig. 6, pressure data are plotted in the circumferential direction. Pressure data measured by Cleary⁹⁾ at $M_\infty = 7.4$ are also shown in

Fig. 6a. Circumferential Pressure; $\alpha = 5^\circ$ Fig. 6b. Circumferential Pressure; $\alpha = 10^\circ$ Fig. 6c. Circumferential Pressure; $\alpha = 15^\circ$

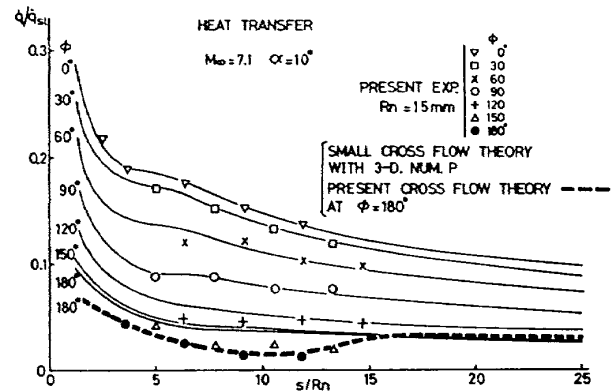
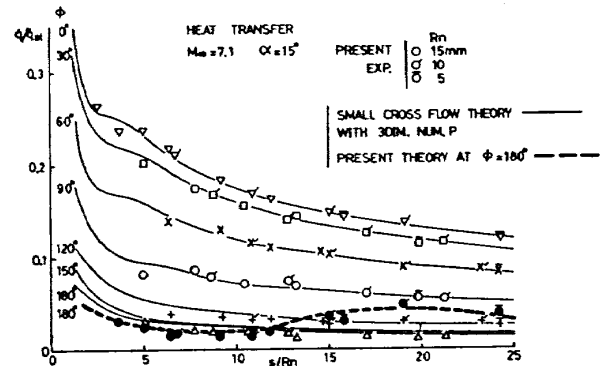
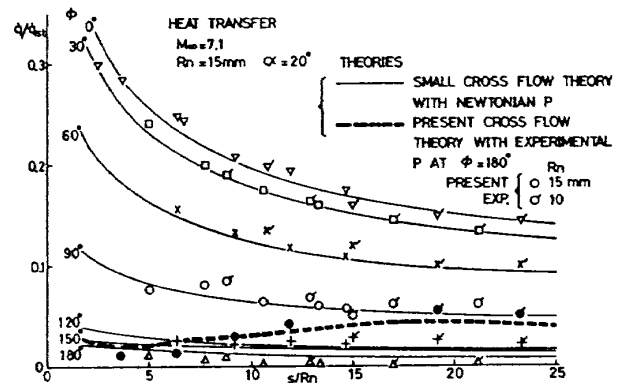
Fig. 6d. Circumferential Pressure; $\alpha=20^\circ$

those figures. The solid lines in these figures are the numerical results described in the next chapter. In Figs. 5 of c_p vs. s/Rn , the measured pressure data for different nose radii line up along a curve at each generator even at the most leeward generator. Also in Figs. 6 of c_p vs. ϕ , pressure data line up along a curve at each longitudinal station. As shown from these figures, adverse pressure gradients in ϕ direction are existing in nowhere at $\alpha=5^\circ$, in leeward regions of $s/Rn \geq 15$ at $\alpha=10^\circ$, of $s/Rn \geq 7.0$ at $\alpha=15^\circ$ and of $s/Rn \geq 4.0$ at $\alpha=20^\circ$. In Fig. 6c of c_p vs. ϕ at $\alpha=15^\circ$, the separation points obtained from the oil flow visualization are indicated. It is obviously seen that the separation occurs a little after the flow experiences an adverse pressure gradient in ϕ direction. This separation point of cross flow is similar to the case of a two-dimensional separation which occurs at a little downstream of the starting point of an adverse pressure gradient in flow direction. Though the separation criterion in two-dimensions is simply given by $\tau_w = \left(\mu \frac{\partial u}{\partial x_s} \right)_w = 0$, the direction, in three-dimensional case, of the wall shear vector to be considered in criterion can not be given a priori, since the flow can take an another direction, if it encounters an adverse pressure gradient in one direction. The ϕ direction is not the correct direction as for in a separation criterion in this sense and the correct direction in a nonconical three-dimensional separation criterion is to be given in the next chapter.

The heat transfer results are presented in Figs. 7a–7e in the normalized form by a stagnation point value against s/Rn . The most remarkable feature of heat transfer data is

that the significant increase of heat transfer along the most leeward generator can be seen for the cases of $\alpha \geq 15^\circ$ where a wide separation is occurring as shown by an oil flow visualization. The heat transfer data for different nose radii along each generator line up on a curve even along the most leeward generator of $\phi=180^\circ$ with a remarkable heat transfer increase.

According to these experimental observa-

Fig. 7a. Heat Transfer Distribution; $M_\infty=7.1$, $\alpha=10^\circ$ Fig. 7b. Heat Transfer Distribution; $M_\infty=7.1$, $\alpha=15^\circ$ Fig. 7c. Heat Transfer Distribution; $M_\infty=7.1$, $\alpha=20^\circ$

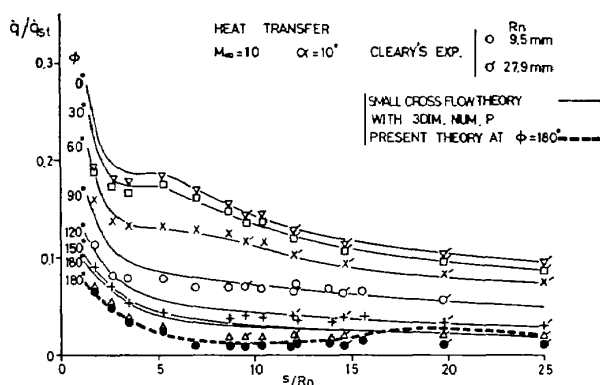


Fig. 7d. Heat Transfer Distribution; $M_\infty=10$, $\alpha=10^\circ$

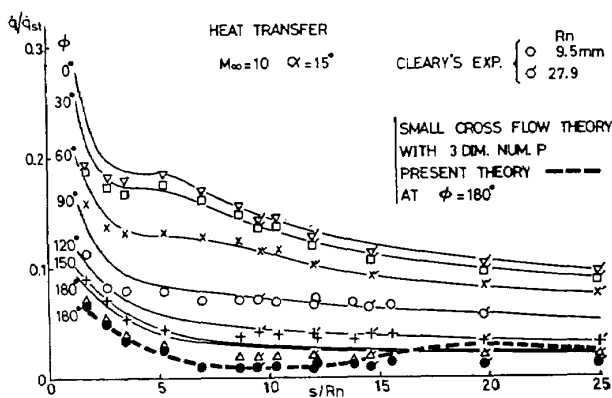


Fig. 7e. Heat Transfer Distribution; $M_\infty=10$, $\alpha=15^\circ$

tions, the significant fact should be pointed out that if the surface length was normalized by Rn , all measured properties for different nose radii become duplicate in a normalized form of heat transfer, surface pressure, shock wave shapes, separated regions and oil streaks. This fact obviously implies the followings about a separated flow; (1) a local Reynolds number effect will be small (2) thickness of a separated viscous layer will be small and the boundary layer approximation can be applicable (3) the viscous interaction effect on inviscid flow will be small and the separable treatment of inviscid flow and boundary layer flow can be applicable as shown in Fig. 1 of the flow model (4) the separated boundary layer will have a similarity rule along the most leeward generator.

III. NUMERICAL ANALYSIS OF THREE-DIMENSIONAL INVISCID FLOW

In this chapter, the inviscid flow behavior in the shock layer over a blunt cone at an angle of attack in a hypersonic flow has been investigated. Comparing with the well known axi-

symmetric flow over a blunt body, the essential difference of a three-dimensional flow derives from the lateral component of a flow velocity and the main effect of this cross flow emerges phenomenally as an adverse pressure gradient in the circumferential direction which would induce the three-dimensional separation of a boundary layer over a leeward surface.

Up to this time, there has been no analytical method to solve a rotational, nonconical inviscid flow in three-dimensions. Hence, the three-dimensional Eulerian equations were solved numerically and the solutions were compared with the experimental results. As for the numerical methods, there have been proposed a number of methods, but the method for this problem has not completely been established yet. In the following section, a short review of these methods and a brief explanation for the method applied in this paper are presented.

3.1. Method of Numerical Analysis

3.1.1. Review of Numerical Methods

Since the angle of attack is chosen moderate in this paper, the subsonic flow behind a detached bow wave is restricted within an axisymmetric flow over a spherical nose and, therefore, the entire three-dimensional flow over a cone surface becomes supersonic. The methods for an axisymmetric flow of subsonic and low-supersonic speeds over a sphere have been well established; namely, the inverse method^{(42),(43)} and the characteristics method^{(44),(45)}. The solutions on a spherical nose can be used as the initial values required for the three-dimensional Eulerian equations governing the three-dimensional supersonic flow over a part of a sphere and a cone surface.

Concerning the direct numerical method to solve the three-dimensional Eulerian equations as an initial value problem, the finite difference method (noncharacteristic) and the characteristics method can be applicable. The later method, however, becomes too complicated in arithmetic formulations to apply for a three-dimensional flow and extensive works have been focused on the former method. Depending on the treatment of basic equations and shock wave, the finite difference methods can be classified into following categories; time-dependent method and steady method; shock capturing method and sharp shock method. Also depending on a finite difference formulation, methods are divided into two types of 2nd-order and 3rd-order accuracy. As for the 2nd-order

scheme, typical methods are the implicit method by Babenko et al.⁴⁵, the single stage integration of Lax-Bendroff type by Moretti et al.³⁰, and the double stages integration of predictor-corrector type by Barnwell³⁰ and MacCormack³¹. By applying a noncentered difference scheme in contrast with the centered one in other methods, MacCormack's method becomes simple in formulation, fast and accurate in computation. In regard to MacCormack's method, MacCormack applied his scheme at first to an unsteady two-dimensional Navier-Stokes equation solved by a time dependent method. The applications of MacCormack's scheme to three-dimensional steady Eulerian equations have been done by Thomas et al.³², Kutler et al.³³ and Moretti et al.³⁴. Thomas et al. solved the case without any embedded shock by the sharp shock method. Kutler et al. and Moretti et al. solved the cases with embedded shock in a shock layer by the shock capturing method and the sharp shock method, respectively. Concerning the boundary condition on the body surface which is most important⁴⁶ for the successful application of the numerical integration scheme, many methods have been proposed. In the predictor-corrector type integration, a two step formula would be applied for the boundary condition which is physically a simple slip condition on a wall. In the above cases of Thomas, Kutler, and Moretti, the boundary condition schemes of Thomas' method, Abbett's method and Barnwell's method were applied, respectively. As the results, Kutler et al. and Moretti et al. obtained stable solutions, Thomas et al., however, have a numerical oscillations after a curvature discontinuity of the wall.

In this paper after these reviewing, the following couple of the methods was employed; MacCormack's 2nd-order noncentered predictor-corrector method applied as a steady method together with a sharp shock treatment and Abbett's method for a wall boundary conditions.

3.1.2. 3-D Steady Eulerian Equations

The axisymmetric flow of subsonic and low-supersonic speed over a spherical nose were solved by the well known inverse method and characteristics method. In the inverse method, the two-dimensional Eulerian equations of elliptic type are solved as an initial value problem by assuming an appropriate shock shape to fit a given body shape iteratively. These solutions provided initial values for the

two-dimensional Eulerian equations of hyperbolic type in a streamline direction which can be solved by the characteristics method. From these solutions on a sphere, the initial values for the three-dimensional Eulerian equations of hyperbolic type in the cone axis direction were obtained.

The Eulerian equations can be described in vector form as

$$\text{Continuity: } \nabla \cdot \rho \vec{V} = 0 \quad (3.1)$$

$$\text{Momentum: } \rho(\vec{V} \cdot \nabla) \vec{V} + \nabla p = 0 \quad (3.2)$$

$$\text{Energy: } \vec{V} \cdot (\nabla p - a^2 \nabla \rho) = 0 \quad (3.3)$$

where eq. (3-3) is introduced from $dS=0$ along a streamline in a shock layer and then this form cannot treat an embedded shock wave in a flow field by a shock capturing way.

By normalizing and stretching the cylindrical coordinates (r, ϕ, z) , the transformed coordinates (X, Y, Z) are defined as

$$\left. \begin{aligned} X &= f\left(\frac{r-r_b}{r_s-r_b}\right) \\ Y &= g\left(\frac{\phi}{\pi}\right) \\ Z &= z \end{aligned} \right\} \quad (3.4)$$

where f and g are single valued functions increasing monotonically

$$\begin{aligned} \text{from} \quad & f(0)=g(0)=0 \\ \text{to} \quad & f(1)=g(1)=1 \end{aligned} \quad (3.5)$$

The basic equations in X, Y, Z coordinates can be described as

$$(\tau \bar{\eta} \rho u_3) \frac{\partial \bar{H}}{\partial Z} + [A] \frac{\partial \bar{H}}{\partial X} + [B] \frac{\partial \bar{H}}{\partial Y} + \bar{E} = 0 \quad (3.6)$$

where

$$\bar{H} = \begin{bmatrix} p \\ \rho \\ u_1 \\ u_2 \\ u_3 \end{bmatrix}, \quad \bar{E} = \rho \begin{bmatrix} \rho a^2 u_1 u_3^2 \\ \rho u_1 u_3^2 \\ -\bar{\eta} u_2^2 \\ \bar{\eta} u_1 u_2 \\ a^2 u_1 u_3 \end{bmatrix}, \quad \bar{\eta} = u_3^2 - a^2 \quad (3.7)$$

and coefficient matrices $[A]$ and $[B]$ are shown in APPENDIX A.

If the axial velocity u_3 is supersonic entirely over the region considered, eq. (3-5) becomes hyperbolic type and can be solved as an initial value problem in Z direction. In general, $u_1 < a$ and $u_2 < a$ and then eq. (3-5) is elliptic type in X, Y directions. Therefore, the solutions in $X-Y$ phase plane are marched down in Z direction with satisfying the conditions on the surrounding boundaries of $X=0, 1$ and $Y=0, 1$ starting from the initial plane where the axial velocity is supersonic.

Since the detailed method to solve these hyperbolic equations is given in Ref. (56), only the outline is described subsequently.

MacCormack's 2nd-order predictor-corrector scheme is given as

Predictor:

$$\begin{aligned} \tilde{H}_{i+1,j,k} = & \bar{H}_{i,j,k} - [A]_{i,j,k}(\bar{H}_{i,j+1,k} - \bar{H}_{i,j,k})\bar{h}_1 \\ & - [B]_{i,j,k}(\bar{H}_{i,j,k+1} - \bar{H}_{i,j,k})\bar{h}_2 - \bar{E}_{i,j,k}\Delta Z \end{aligned} \quad (3.8)$$

Corrector:

$$\begin{aligned} \dot{H}_{i+1,j,k} = & \frac{1}{2} \left\{ \bar{H}_{i,j,k} + \tilde{H}_{i+1,j,k} - [\tilde{A}]_{i+1,j,k}(\tilde{H}_{i+1,j,k} \right. \\ & - \tilde{H}_{i+1,j-1,k})\tilde{h}_1 - [\tilde{B}]_{i+1,j,k}(\tilde{H}_{i+1,j,k} \\ & \left. - \tilde{H}_{i+1,j,k-1})\tilde{h}_2 - \tilde{E}_{i+1,j,k}\Delta Z \right\} \end{aligned} \quad (3.9)$$

where $\partial H/\partial X$ and $\partial H/\partial Y$ are approximated by forward and backward finite differences in predictor and corrector, respectively.

In the sharp shock method, the boundary conditions on a shock wave ($X=1$) are given from conservation equations of mass flow, momentum, energy and tangent velocity on a shock wave surface as follows;

$$\begin{aligned} \frac{\partial r_s}{\partial z} = & \frac{1}{u_{3\infty}^2 - V_{\infty n}^2} \left[u_{3\infty} \left(u_{1\infty} - \frac{u_{2\infty}}{r_s} \frac{\partial r_s}{\partial \phi} \right) \right. \\ & + V_{\infty n} \sqrt{\left(u_{1\infty} - \frac{u_{2\infty}}{r_s} \frac{\partial r_s}{\partial \phi} \right)^2 + (u_{3\infty}^2 - V_{\infty n}^2)} \\ & \left. \cdot \left\{ 1 + \left(\frac{1}{r_s} \frac{\partial r_s}{\partial \phi} \right)^2 \right\} \right] \end{aligned} \quad (3.10)$$

$$V_{\infty n} = \sqrt{\frac{\rho(p-p_\infty)}{\rho_\infty(\rho-\rho_\infty)}} \quad (3.11)$$

$$\frac{\rho}{\rho_\infty} = \left(\frac{\gamma+1}{\gamma-1} \right) \frac{p + \left(\frac{\gamma-1}{\gamma+1} \right) p_\infty}{p + \left(\frac{\gamma+1}{\gamma-1} \right) p_\infty} \quad (3.12)$$

$$\left. \begin{aligned} u_1 &= u_{1\infty} + b_1 \\ u_2 &= u_{2\infty} - \frac{b_1}{r_s} \frac{\partial r_s}{\partial \phi} \\ u_3 &= u_{3\infty} - b_1 \frac{\partial r_s}{\partial z} \end{aligned} \right\} \quad (3.13)$$

These four conservation equations are supplemented by predictor-corrector for pressure to close the relations.

In the Abbett's method for the boundary conditions on a wall, the predictor (3-8) is applied first at $X=0$. The predicted velocity $\tilde{V}_{i+1,j,k}$ is rotated to flow along a wall by assuming isentropic waves fictitiously; the rotation angle $\Delta\theta$ is

$$\Delta\theta = \sin^{-1} \left(\frac{\tilde{V}_{i+1,j,k} \cdot \vec{n}_{\text{wall}}}{|\tilde{V}_{i+1,j,k}|} \right) \quad (3.14)$$

Pressure after the waves is

$$\begin{aligned} p_{i+1,j,k} = & \tilde{p}_{i+1,j,k} \left[1 - \left(\frac{\gamma \tilde{M}^2}{\tilde{\beta}} \right) \Delta\theta \right. \\ & \left. + \gamma \tilde{M}^2 \left\{ \frac{(\gamma+1)\tilde{M}^4 - 4\tilde{\beta}^2}{4\tilde{\beta}^4} \right\} \Delta\theta^2 \right] \end{aligned} \quad (3.15)$$

Density and velocity are given from conservation equations of entropy and energy along a wall as

$$\rho_{i+1,j,k} = \rho_{\text{initial}} \left(\frac{p_{i+1,j,k}}{p_{\text{initial}}} \right)^{1/\gamma} \quad (3.16)$$

$$V_{i+1,j,k} = \sqrt{V_{\infty}^2 + \frac{2\gamma}{\gamma-1} \left(\frac{p_\infty}{\rho_\infty} - \frac{p_{i+1,j,k}}{\rho_{i+1,j,k}} \right)}$$

$$u_{1\ i+1,j,k} = V_{i+1,j,k} (\tilde{u}_{1\ i+1,j,k} - b_2) / b_3$$

$$u_{2\ i+1,j,k} = V_{i+1,j,k} \left(\tilde{u}_{2\ i+1,j,k} + \frac{b_2}{r_b} \frac{\partial r_b}{\partial \phi} \right) / b_3$$

$$u_{3\ i+1,j,k} = V_{i+1,j,k} \left(\tilde{u}_{3\ i+1,j,k} + b_2 \frac{\partial r_b}{\partial z} \right) / b_3$$

(3.17)

The boundary conditions in Y direction are given by symmetry conditions at $Y=0$ and 1 as follows;

$$\left. \begin{aligned} \frac{\partial p}{\partial Y} = \frac{\partial \rho}{\partial Y} = \frac{\partial u_1}{\partial Y} = \frac{\partial u_3}{\partial Y} = 0 \\ u_2 = 0, \quad \frac{\partial u_2}{\partial Y} = \frac{\partial u_2}{\partial \phi} / \frac{\partial g}{\partial \phi} \end{aligned} \right\} \quad (3.18)$$

For applying eqs. (3-8) and (3-9), a step size Z should be determined from a stability condition for a numerical scheme. However, no rigorous limit has yet been established for a three-dimensional nonlinear partial differential equations. Therefore, in this paper the simultaneous applications of the amplification matrix method⁽⁷⁾ have been made for two-dimensional linearized homogeneous equations in $Z-X$ and $Z-Y$ phase planes.

The two-dimensional linearized homogeneous forms corresponding to the basic equations (3-5) are

$$\frac{\partial \tilde{H}}{\partial Z} + [C] \frac{\partial \tilde{H}}{\partial X} = 0 \quad (3.19)$$

$$\frac{\partial \tilde{H}}{\partial Z} + [D] \frac{\partial \tilde{H}}{\partial Y} = 0 \quad (3.20)$$

After applying MacCormack's scheme for these equations, H is expressed by Fourier expansion form in X and Y . Then the amplification matrix for these finite difference equations is easily obtained. Applying the von Neuman's

stability condition⁴⁷⁾, the stable step size Z is determined from this amplification matrix as follows;

$$\text{for eq. (3.19), } \Delta Z \leq \Delta X / \lambda_C \quad (3.21)$$

$$\text{for eq. (3.20), } \Delta Z \leq \Delta Y / \lambda_D \quad (3.22)$$

Characteristics equations for [C] and [D] are

$$\left. \begin{aligned} \det([C] - \lambda_C[I]) &= 0 \\ \det([D] - \lambda_D[I]) &= 0 \end{aligned} \right\} \quad (3.23)$$

These provide eigenvalues λ_C and λ_D as

$$\lambda_{C1} = \frac{1}{u_3} \left(u_1 \frac{\partial f}{\partial r} + \frac{u_2}{r} \frac{\partial f}{\partial \phi} + u_3 \frac{\partial f}{\partial z} \right) \quad (3.24)$$

$$\begin{aligned} \lambda_{C2} &= \frac{\partial f}{\partial z} + \frac{1}{\bar{\eta}} \left[u_3 \left(u_1 \frac{\partial f}{\partial r} + \frac{u_2}{r} \frac{\partial f}{\partial \phi} \right) \right. \\ &\quad \left. \pm \alpha \sqrt{\left(u_1 \frac{\partial f}{\partial r} + \frac{u_2}{r} \frac{\partial f}{\partial \phi} \right)^2 + \bar{\eta} \left[\left(\frac{\partial f}{\partial r} \right)^2 + \left(\frac{1}{r} \frac{\partial f}{\partial \phi} \right)^2 \right]} \right] \end{aligned} \quad (3.25)$$

$$\lambda_{D1} = \frac{1}{u_3} \frac{u_2}{r} \frac{\partial g}{\partial \phi} \quad (3.26)$$

$$\lambda_{D2} = \frac{1}{r\bar{\eta}} (u_2 u_3 \pm \sqrt{\bar{\eta} + u_2^2}) \frac{\partial g}{\partial \phi} \quad (3.27)$$

Here, λ_{C1} and λ_{D1} are corresponding to the streamline directions in $X-Z$ and $Y-Z$ phase planes, respectively, since the angle between a streamline and Z axis in each phase plane is given as

$$\begin{aligned} \theta_{XZ} &= \tan^{-1} \frac{\bar{V} \cdot df}{u_3} \\ &= \frac{1}{u_3} \left(u_1 \frac{\partial f}{\partial r} + \frac{u_2}{r} \frac{\partial f}{\partial \phi} + u_3 \frac{\partial f}{\partial z} \right) = \lambda_{C1} \end{aligned}$$

$$\theta_{YZ} = \tan^{-1} \frac{\bar{V} \cdot dg}{u_3} = \frac{1}{u_3} \frac{u_2}{r} \frac{\partial g}{\partial \phi} = \lambda_{D1}$$

Then, λ_{C2} and λ_{D2} which are the solutions of characteristics equations should be characteristics directions of 1st and 2nd families for eqs. (3-19) and (3-20). Therefore, either value of λ_{C2} for 1st and 2nd families, λ_{Cm} , is always greater than λ_{C1} for a streamline, and λ_{Dm} is greater than λ_{D1} .

The minimum value of ΔZ given by eqs. (3-21) and (3-22) is obtained by applying the following equation at all mesh point in $X-Y$ phase plane;

$$\Delta Z_m = (\Delta X / \lambda_{Cm}, \Delta Y / \lambda_{Dm})_{\text{minimum}}$$

For the three-dimensional nonlinear equation, the stable step size is given by the substantial fraction of ΔZ_m as

$$\Delta Z = K \cdot \Delta Z_m \quad (3.28)$$

where $K=0.9$ is selected for the present calculation.

This stability condition shows that the finite difference step cannot exceed the characteristics line at each point.

The same results as eq. (3-24) ~ (3-27) were obtained by Kutler et al.³³⁾ where they used an enthalpy conservation equation as an energy equation in order to apply a shock capturing method.

3.2. Inviscid Flow Solutions

Numerical computations were conducted for the conditions as follows;

Flow conditions of

$$M_\infty = 7.1, 10.0$$

$$\gamma = 1.4$$

$$\alpha = 0^\circ, 5^\circ, 10^\circ, 15^\circ$$

Numerical mesh (equally spaced) of

$$\Delta X = 1/24 : \Delta r = (r_s - r_b)/24$$

$$\Delta Y = 1/24 : \Delta \phi = \pi/24$$

3.2.1. Shock wave and shock layer

The shock wave patterns calculated at $\alpha=0^\circ, 5^\circ, 10^\circ, 15^\circ$ in $M_\infty=7.1$ are shown on a symmetric plane of $\phi=0^\circ, 180^\circ$ in Fig. 3b where length is normalized by Rn . Compared experimental results are for two different nose radii in order to investigate the local Reynolds number effect.

The numerical solutions agree quite well with experimental results at any angle of attack and no effect of the nose radius can be seen. In the same figure, the shock wave angles for a sharp cone at $\alpha=0^\circ, 5^\circ$, and 10° in $M_\infty=7$ calculated numerically by Babenko et al.⁴⁸⁾ are presented. For $\alpha=0^\circ$, the effect of the nose bluntness is still obviously seen. The results for a blunt cone at $\alpha=5^\circ$ and 10° in the windward side agree with the shock wave angle for a sharp cone in the region of $z/Rn \leq 15$, since the streamlines passed through the bow shock wave have concentrated into a thin entropy layer near the wall rapidly. The results for $\alpha=5^\circ$ and 10° in the leeward side have not shown a conical behavior yet, since the streamlines passed a strong shock spread widely in the shock layer which make the flow behave nonconically. The flow field on the most leeward plane of a sharp cone has essentially different properties with the flow field of a blunt cone, since a vortical singularity should be considered on the plane. However, for the small angle of attack as $\alpha \leq 10^\circ$, this singularity is still on the wall⁴⁹⁾ and its effect will be small. Babenko et al. did not calculate the large attack angle case of $\alpha/\theta_c \geq 1$ and, there-

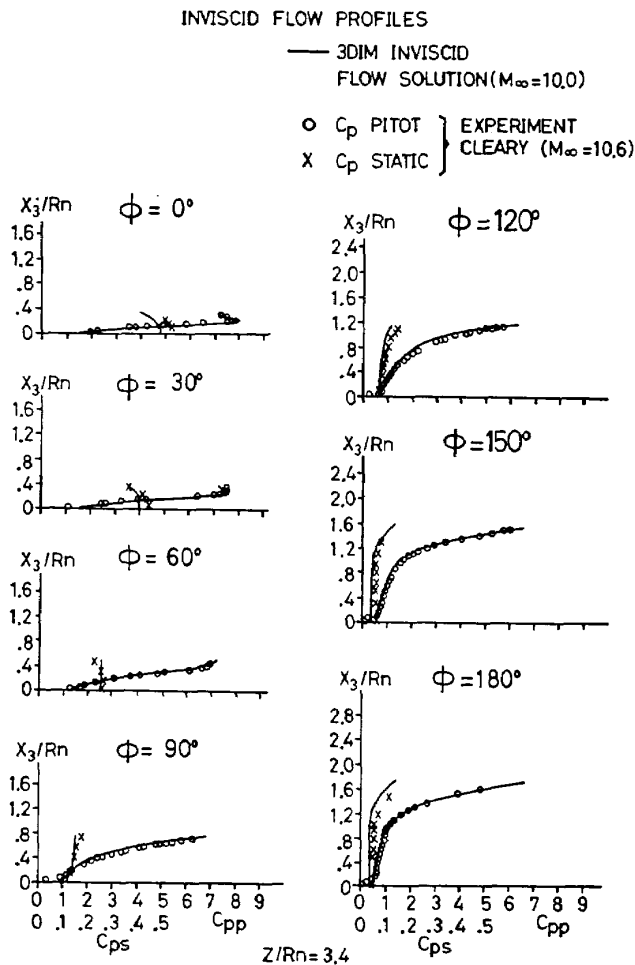


Fig. 8a. Pitot and Static Pressure; $z/Rn=3.4$

fore, they did not obtain a vortical singularity lifted off the surface.

In Fig. 8, the static and pitot pressure distributions in a shock layer are shown compared with Cleary's experimental data⁽⁸⁾ measured normal to the surface at two different axial stations of $z/Rn=3.4$ and 14.7 at $M_\infty=10.6$.

As for the static pressure profiles, the agreement between numerical and experimental results is quite good except for the most windward results ($\phi=0^\circ$) where a thick boundary layer developed on a spherical nose may affect the static pressure in experiments as to be discussed in the next subsection.

As for the pitot pressure profile, the agreement between numerical and experimental results is quite good at the upstream station and fairly good at the downstream station. A very thin entropy layer can be seen near the wall as a steep pitot pressure gradient in a windward side of the downstream station where the streamlines passed through a strong bow shock wave around a stagnation point concentrate near the wall.

Very near the wall, pitot probe data shift

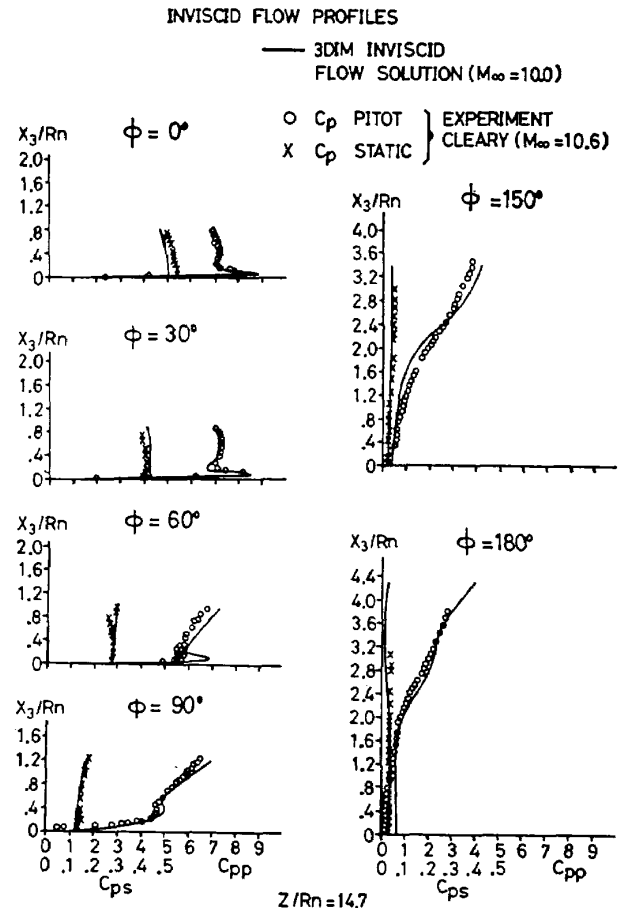


Fig. 8b. Pitot and Static Pressure; $z/Rn=14.7$

toward zero, but numerical results do not. This is obviously due to a boundary layer effect which increases entropy of a flow there. However, the widely shifted layer up to $x_s/Rn \sim 1.0$ at $\phi=180^\circ$ of the downstream station will not be due to a boundary layer, but due to a weak cross flow shock wave embedded in a shock layer near the wall which can be surmised from Fig. 10d of the cross flow Mach number contours. Figs. 9c, d and 10c, d show calcu-

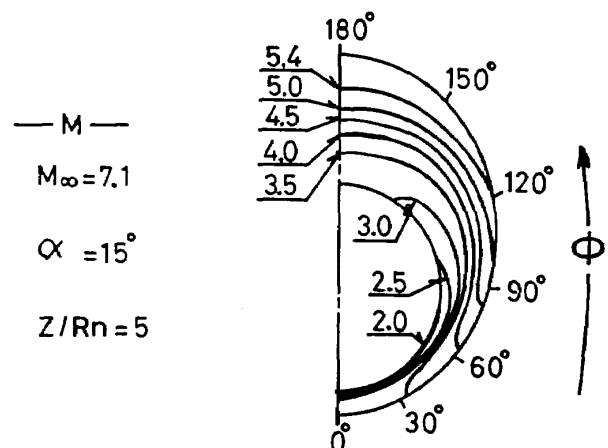


Fig. 9a. M Number Contour; $M=7.1$, $z/Rn=5$

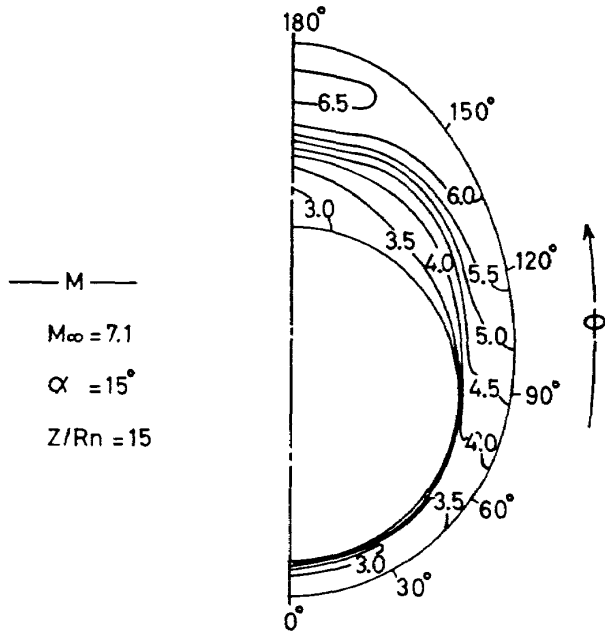


Fig. 9b. M Number Contour; $M=7.1$, $z/Rn=15$

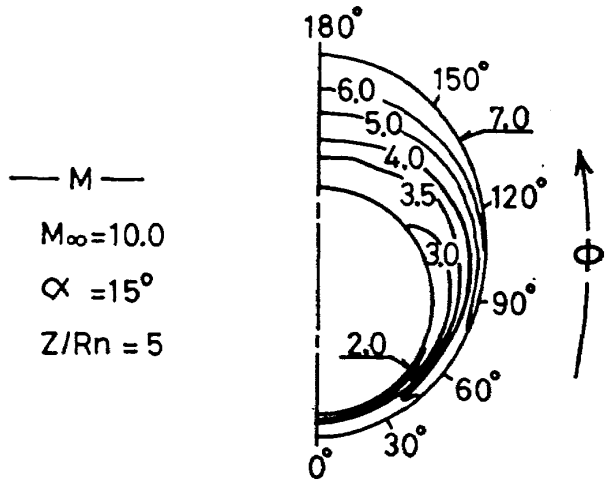


Fig. 9c. M Number Contour; $M=10.0$, $z/Rn=5$

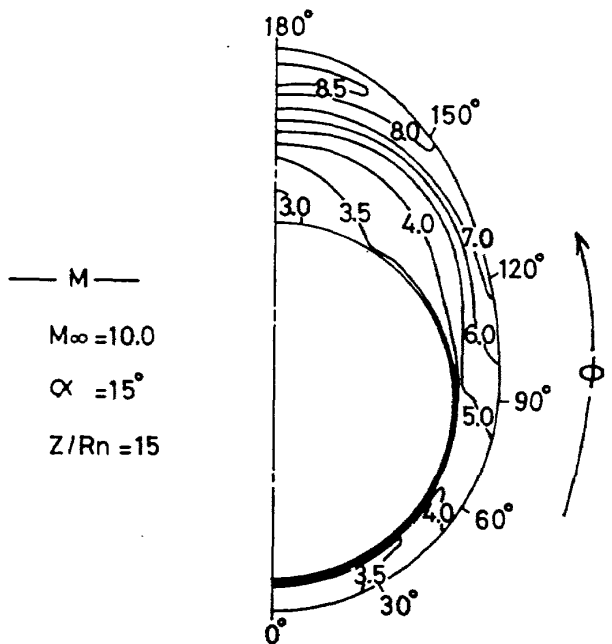


Fig. 9d. M Number Contour; $M=10.0$, $z/Rn=15$

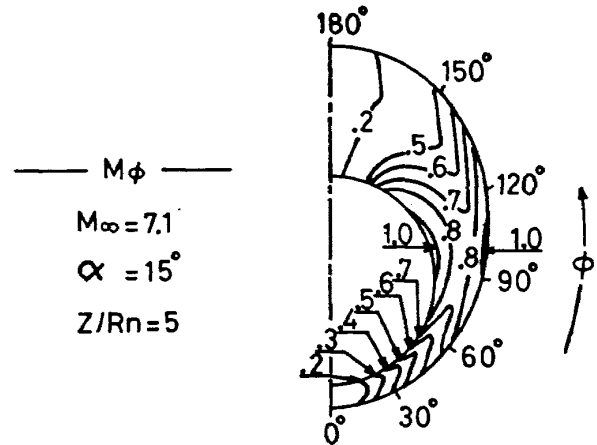


Fig. 10a. $M\phi$ Number Contour; $M=7.1$, $z/Rn=5$

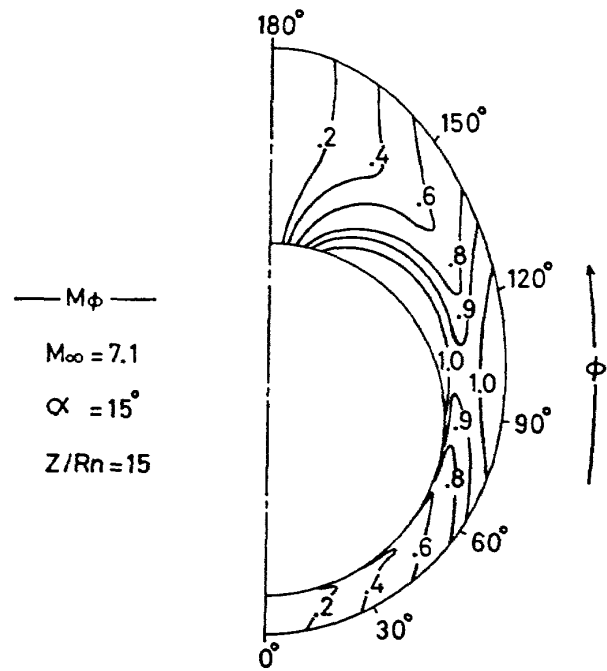


Fig. 10b. $M\phi$ Number Contour; $M=7.1$, $z/Rn=15$

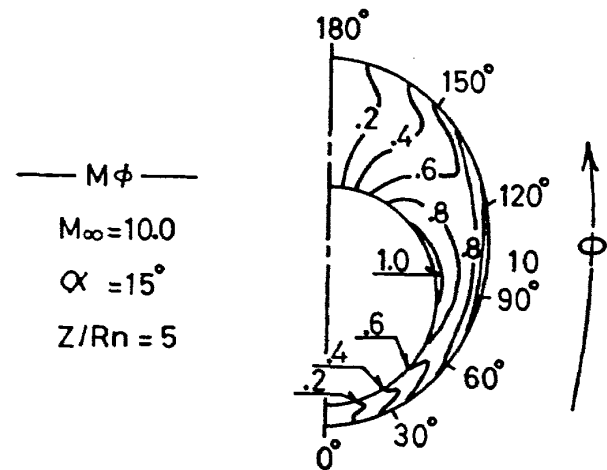


Fig. 10c. $M\phi$ Number Contour; $M=10.0$, $z/Rn=5$

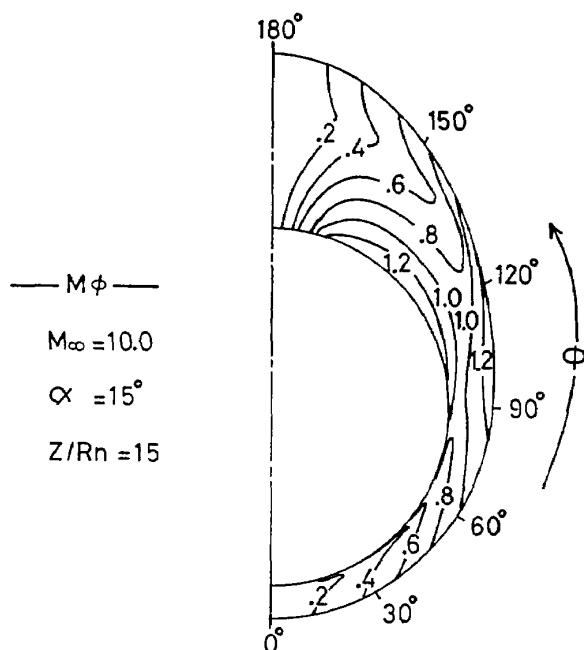


Fig. 10d. $M\phi$ Number Contour; $M=10.0$, $z/Rn=15$

lated Mach number and cross flow Mach number contours in $X-Y$ plane at $z/Rn=5.0$ and 15.0 in $M_\infty=10.0$. Though at $z/Rn=5.0$, a cross flow becomes supersonic only in a very narrow region, the region of supersonic cross flow at $z/Rn=15.0$ widely spreads up to $\phi \sim 165^\circ$ near the wall where a cross flow is decelerated to subsonic speed with so large Mach number gradient that a weak embedded shock wave could be induced in an actual flow; in the present numerical solutions, an embedded shock wave cannot be obtained due to the isentropic assumption along a streamline. The supersonic cross flow region expands over one-fourth of the shock layer at $z/Rn=15$ which corresponds approximately to the region of shifted pitot probe data ($x_s/Rn \sim 1.0$) at $\phi=180^\circ$.

3.2.2. Surface Pressure and Surface Streamline

Fig. 11 shows a surface pressure distribution on a hemisphere and along the most windward generator of the connected cone with $\theta_c=15^\circ$ at several angles of attack. Numerical solutions are compared with the present experimental results and with Cleary's results. The Reynolds number based on a nose diameter d are 6.3×10^4 and 5.3×10^5 in the present and in the Cleary's case, respectively.

The agreement of numerical solution with experimental results is quite good except for the Cleary's case in $\theta > 60^\circ$. In order to check the boundary layer interaction effect, the lami-

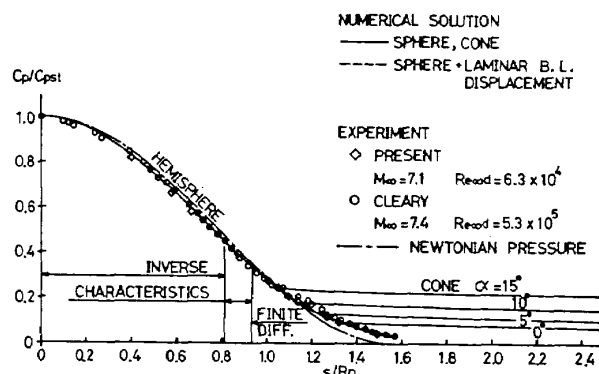


Fig. 11. Surface Pressure on Sphere

nar boundary layer equations with the similarity assumption are solved for Cleary's conditions by using the numerical pressure solutions and isentropic condition along the outer edge of boundary layer. Attaching the displacement thickness of the obtained boundary layer to the surface of sphere, an inviscid flow was recalculated and the resulted surface pressure was shown by a dotted line in the same figure. As seen from this figure, the interaction effect with a laminar boundary layer is very small. Consequently, the discrepancy with Cleary's data may imply a transition to turbulent boundary layer around $\theta \sim 60^\circ$ ($s/Rn=1.05$), though the local Reynolds number of 2.8×10^5 at this point is a little smaller as the transition Reynolds number which is about the order of 10^6 for a smooth surface in this conditions.

In Fig. 5, the numerical results of pressure distribution on a cone surface along generators at angles of attack of $\alpha=0^\circ, 5^\circ, 10^\circ, 15^\circ$ at $M_\infty=7.1$ are shown compared with the present and Cleary's experimental results which include the four different nose radii. The numerical solutions agree well with experimental results for any angle of attack and for any nose radius. Also in Fig. 5, the results for a sharp cone calculated by Babenko et al.⁴⁵⁾ numerically are shown for $\alpha=0^\circ, 5^\circ$, and 10° . The comparison of both results for a sharp cone and a blunt cone shows the almost exact agreement except for $\phi=180^\circ$ at $\alpha=10^\circ$. For $\alpha \leq 10^\circ$, the remarkable effect of a vortical singularity cannot be seen in the pressure distributions as in the shock shape, since the attack angle is small. The results compared with the Cleary's data in the windward side near the sphere-cone junction show a little discrepancy which can be explained by the reduced curvature of a sphere due to the thick displacement on it as mentioned above which

affects the overexpansion-recompression process on a cone surface caused by a curvature discontinuity at the junction. The agreement of the solutions with the data for different nose radii on the leeward surface implies that the boundary layer thickness on the surface is not so thick as to affect the pressure distribution, even if the wide separation is taking place as shown experimentally in pictures of oil flow visualization of Fig. 4.

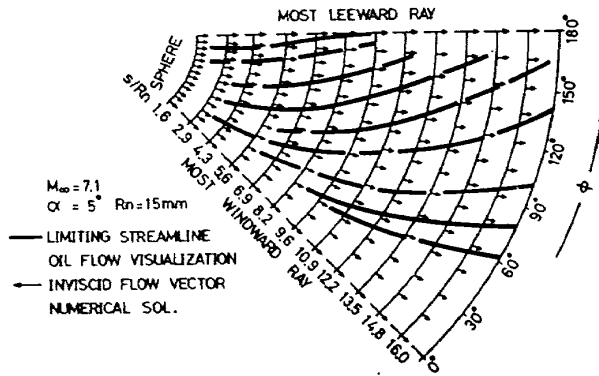


Fig. 12a. Oil Streaks and Inviscid Vectors;
 $\alpha=5^\circ$

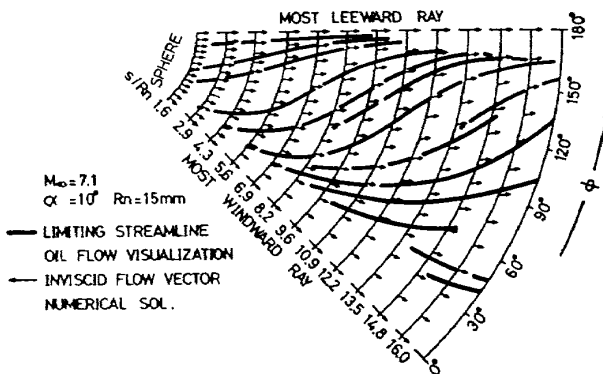


Fig. 12b. Oil Streaks and Inviscid Vector;
 $\alpha=10^\circ$

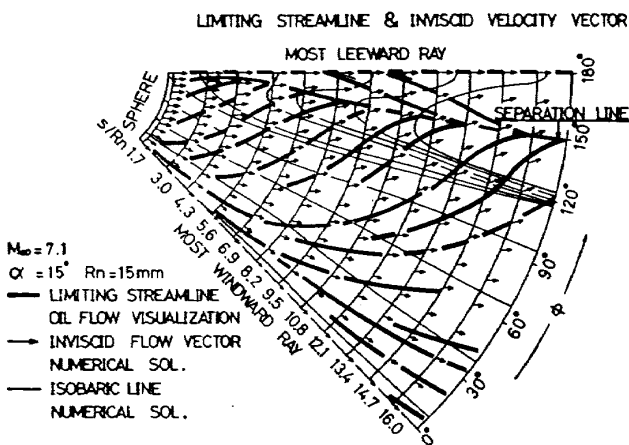


Fig. 12c. Oil Streaks and Inviscid Vector;
 $\alpha=15^\circ$

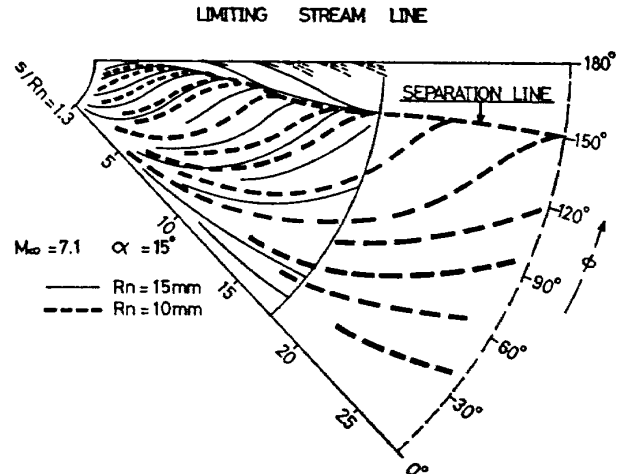


Fig. 12d. Oil Streaks for Different R_n

In Fig. 6, solutions of circumferential pressure distribution on a cone are shown at several axial stations. The agreement with experimental results is quite good. For the case of $\alpha=15^\circ$, the separation points obtained from the picture of oil flow visualization are indicated. These points are locating at a little over the minimum pressure point in circumferential distribution. Here, it can be seen that the numerical solutions as well as experimental data show a pressure peak at $\phi=180^\circ$ clearly. This adverse pressure increase is corresponding to the decrease of cross flow Mach number from supersonic to subsonic as shown in Figs. 10a, b. Since the gradient of decreasing M_ϕ is smaller than the case of $M_\infty=10$ in Fig. 10d, the presence of an embedded shock wave is not clear at $M_\infty=7.1$.

In Fig. 12, numerical solutions of velocity vectors of an inviscid flow over a cone surface are shown comparing with oil streaks on a surface. At any angle of attack, inviscid velocity vectors have almost the same directions as the oil streaks in the region of $\phi=0^\circ\sim 120^\circ$. In the region of $\phi>120^\circ$, both directions of inviscid flow velocity vectors and oil streaks become disagreed even in the case of $\alpha=5^\circ$ where no separation takes place. This discrepancy in the directions exhibits a twist of a flow direction across a boundary layer and occurrence of the secondary flow.

In Fig. 12c, also shown are isobaric lines drawn from the numerical solutions. It can be seen clearly that the separation line is running approximately in parallel with the trough of isobaric line and that a flow separates a little after it experiences an adverse pressure gradient in the direction normal to the trough. From this relative location of a separation

line and a trough, the separation criterion for three-dimensional boundary layer can be drawn as

$$(\tau_p)_w = \left(\mu \frac{\partial V_P}{\partial X_s} \right)_w = 0 \quad (3.31)$$

where the subscript p denotes the normal component to the trough of isobaric lines. Obviously, this criterion can cover the case of two-dimensional separation.

IV. THEORETICAL ANALYSIS OF THREE-DIMENSIONAL BOUNDARY LAYER AND HEAT TRANSFER

In this chapter, the three-dimensional boundary layer equations are analyzed and heat transfer distributions are obtained over a blunt cone at an angle of attack with special attentions on the leeward region. The outer edge conditions are given by the inviscid flow solutions.

4.1. Basic Equations

The three-dimensional boundary layer equations in a curvilinear coordinate system (x_1, x_2, x_3) are written as

Continuity:

$$\frac{\partial}{\partial x_1}(h_2 \rho u) + \frac{\partial}{\partial x_2}(h_1 \rho v) + \frac{\partial}{\partial x_3}(h_1 h_2 \rho w) = 0 \quad (4.1)$$

x_1 Momentum:

$$\begin{aligned} \rho \frac{u}{h_1} \frac{\partial u}{\partial x_1} + \rho \frac{v}{h_2} \frac{\partial u}{\partial x_2} + \rho w \frac{\partial u}{\partial x_3} + \rho \frac{uv}{h_1 h_2} \frac{\partial h_1}{\partial x_2} \\ - \frac{\rho v^2}{h_1 h_2} \frac{\partial h_2}{\partial x_1} = -\frac{1}{h_1} \frac{\partial p}{\partial x_1} + \frac{\partial}{\partial x_3} \left(\mu \frac{\partial u}{\partial x_3} \right) \end{aligned} \quad (4.2)$$

x_2 Momentum:

$$\begin{aligned} \rho \frac{u}{h_1} \frac{\partial v}{\partial x_1} + \rho \frac{v}{h_2} \frac{\partial v}{\partial x_2} + \rho w \frac{\partial v}{\partial x_3} + \rho \frac{uv}{h_1 h_2} \frac{\partial h_2}{\partial x_1} \\ - \frac{\rho u^2}{h_1 h_2} \frac{\partial h_1}{\partial x_2} = -\frac{1}{h_2} \frac{\partial p}{\partial x_2} + \frac{\partial}{\partial x_3} \left(\mu \frac{\partial v}{\partial x_3} \right) \end{aligned} \quad (4.3)$$

Energy:

$$\begin{aligned} \rho \frac{u}{h_1} \frac{\partial H}{\partial x_1} + \rho \frac{v}{h_2} \frac{\partial H}{\partial x_2} + \rho w \frac{\partial H}{\partial x_3} \\ = \frac{\partial}{\partial x_3} \left[\frac{\mu}{Pr} \frac{\partial H}{\partial x_3} + \left(1 - \frac{1}{Pr} \right) \mu \left(u \frac{\partial u}{\partial x_3} + v \frac{\partial v}{\partial x_3} \right) \right] \end{aligned} \quad (4.4)$$

where x_3 is the length measured normal to the surface and hence $h_3=1$.

Now, consider the inviscid streamline coordinate system as curvilinear coordinate system where x_1 is the coordinate taken along a inviscid flow streamline at the outer edge of boundary layer and then x_2 becomes a coordinate normal to x_1 and tangent to the wall. Consequently, v becomes the secondary flow

across a boundary layer against the inviscid streamline; in this chapter, v is called a cross flow velocity.

The cross flow in a boundary layer occurs along a curved inviscid streamline on the boundary layer edge (this is called "inviscid surface streamline" in the subsequent section) in order to balance a centrifugal force with a pressure gradient in lateral direction. The eq. (4-3) on the boundary layer edge gives

$$\rho_e \kappa_e u_e^2 = \frac{1}{h_2} \frac{\partial p}{\partial x_2} \quad (4.5)$$

Since the lateral pressure gradient of right hand side is considered invariable across a boundary layer, the lateral curvature of streamline κ should become larger near the wall. Hence, a cross flow v is induced.

As seen in Fig. 12, a cross flow velocity component becomes remarkable in the leeward side of $\phi > 120^\circ$, since the inviscid flow rolled up toward the leeward meridian plane should curve on a lee-surface to flow in parallel with a generator. However, in the windward and sideward region of $\phi \leq 120^\circ$, a cross flow component is small, since the curvature κ_e is small and viscosity delays the conduction of the curvature effect.

4.2. Small Cross Flow Approximation

4.2.1. Axisymmetric Analogy

The basic equations (4-1)–(4-4) can be simplified by the small cross flow approximation which will be applicable in the windward and sideward region as mentioned in the previous section.

Neglecting all terms which are involving v and its derivative, eqs. (4-1)–(4-4) are written in the streamline coordinate system as

$$\frac{1}{h_2} \frac{\partial}{\partial x} (h_2 \rho u) + \frac{\partial}{\partial x_3} (\rho w) = 0 \quad (4.6)$$

$$\rho u \frac{\partial u}{\partial x} + \rho w \frac{\partial u}{\partial x_3} = -\frac{\partial p}{\partial x} + \frac{\partial}{\partial x_3} \left(\mu \frac{\partial u}{\partial x_3} \right) \quad (4.7)$$

$$\begin{aligned} \rho u \frac{\partial H}{\partial x} + \rho w \frac{\partial H}{\partial x_3} \\ = \frac{\partial}{\partial x_3} \left[\frac{\mu}{Pr} \frac{\partial H}{\partial x_3} + \left(1 - \frac{1}{Pr} \right) \mu u \frac{\partial u}{\partial x_3} \right] \end{aligned} \quad (4.8)$$

where x is the length measured along an inviscid surface streamline x_1 and then $\frac{1}{h_1} \frac{\partial}{\partial x_1} = \frac{\partial}{\partial x}$.

As obviously seen¹⁾, these eqs. (4-6)–(4-8) are exactly the same as axisymmetric boundary layer equations over a body of revolution with radius $r(x) = h_2$. Using this axisymmetric analogy, heat transfer to a surface can be obtained by applying the well known correlation equa-

tion presented by Lees¹⁹ for an axisymmetric blunt body with a local similarity assumption as

$$\frac{\dot{q}_w}{\dot{q}_{wst}} = \frac{\frac{p}{p_{st}} \frac{u_e}{V_\infty} r \sqrt{Rn}}{2 \sqrt{\frac{1}{V_\infty} \left(\frac{du_e}{d\theta} \right)_{st}} \int \frac{p}{p_{st}} \frac{u_e}{V_\infty} r^2 dx} \quad (4.9)$$

where r should be replaced by h_2 for the present case and $(du_e/d\theta)_{st}$ is given by Lees as

$$\left(\frac{du_e}{d\theta} \right)_{st} = V_\infty \sqrt{\frac{\gamma-1}{\gamma} \left\{ 1 + \frac{1}{(\gamma-1)M_\infty^2} \right\} \left(1 - \frac{1}{\gamma M_\infty^2} \right)} \quad (4.10)$$

For applying eq. (4-9), the numerical solution of the external inviscid flow can be used to give p, u_e, h_2 and an inviscid surface streamline geometry. Instead of determining a streamline geometry and h_2 numerically, the Newtonian approximation method proposed by DeJarnette¹⁷ was employed where the direction of an inviscid flow was determined by Newtonian flow concept. By this method, the geometry of an inviscid surface streamline and h_2 can be given analytically from a vector analysis (as shown in APPENDIX B in detail) as

$$\left(\frac{r_b}{Rn} \right)_{s1} = (\cos \theta_c) \left(\frac{\tan \frac{\hat{\phi}_i}{2}}{\tan \frac{\hat{\phi}}{2}} \right)^{(\sin 2\theta_c/2 \tan \alpha)} \left(\frac{\sin \hat{\phi}_i}{\sin \hat{\phi}} \right) \sin^2 \theta_c \quad (4.11)$$

$$\frac{h_2}{Rn} = \left(\frac{r_b}{Rn} \right)_{s1} \left(\frac{\sin \hat{\phi}}{\sin \hat{\phi}_i} \right) \frac{\sin^2 \hat{\phi}_i + (\cos \hat{\phi}_i \cos \alpha + \tan \theta_c \sin \alpha)^2}{\sqrt{\sin^2 \hat{\phi} + (\cos \hat{\phi} \cos \alpha + \tan \theta_c \sin \alpha)^2}} \quad (4.12)$$

where the cylindrical coordinate $(r_{b1}, \hat{\phi}, z)$ on a cone surface provides the streamline geometry starting from a point of $\hat{\phi} = \hat{\phi}_i$ at the sphere-cone junction.

Using eqs. (4-11), (4-12) together with numerical solutions for p and u_e , eq. (4.9) was calculated for $\alpha = 5^\circ, 10^\circ$ and 15° . For the case of $\alpha = 20^\circ$, the inviscid flow solutions could not be obtained, since the condition $\bar{\eta} = u_s^2 - a^2 > 0$ is not satisfied at the initial data plane located at the sphere-cone junction for the three-dimensional finite difference calculation. This is the limitation of the present theoretical approach and this limitation is originally derived from the difficulty of solving the three-dimensional subsonic flow field which will expand over the cone surface at the larger angle of attack. Hence, for the case of $\alpha = 20^\circ$, the

modified Newtonian pressure distribution combined with an isentropic flow assumption along the boundary layer edge are used to give p/p_{st} and u_e/V_∞ in the following form as introduced by Lees;

$$\frac{p}{p_{st}} = \left(1 - \frac{1}{\gamma M_\infty^2} \right) \cos^2 \theta_{fn} + \frac{1}{\gamma M_\infty^2} \quad (4.13)$$

$$\frac{u_e}{V_\infty} = \sqrt{\left\{ 1 + \frac{2}{(\gamma-1)M_\infty^2} \right\} \left\{ 1 - \left(\frac{p}{p_{st}} \right)^{(\gamma-1)/\gamma} \right\}} \quad (4.14)$$

where θ_{fn} is the angle between a free stream direction and a normal direction to the wall and is given by

$$\cos \theta_{fn} = -\frac{\bar{V}_\infty \cdot \bar{n}}{V_\infty} = \sin \theta_c \cos \alpha - \cos \theta_c \sin \alpha \cos \hat{\phi} \quad (4.15)$$

The region where the right hand side of eq. (4-15) becomes negative means an unwetted surface in the leeward side of a cone. This boundary is given by

$$\phi_{wet} = \pi - \cos^{-1} \left(\frac{\tan \theta_c}{\tan \alpha} \right)$$

In the unwetted region of $\phi > \phi_{wet}$, flow was assumed to have values at $\phi = \phi_{wet}$.

4.2.2. Heat Transfer Solutions

In Fig. 7, the calculated heat transfer distributions by eq. (4-9) are shown compared with experimental results for different α, Rn, M_∞ and Re_∞ . For any conditions, the calculated values agree quite well with experimental results in the region of $\phi < 120^\circ$ where the small cross flow approximation is ensured. The nose bluntness effect is well exhibited for $\alpha = 10^\circ$ and 15° owing to the accurate edge conditions given by the inviscid flow solutions. However, in the region of $\phi > 120^\circ$ where a cross flow component is not negligible, results by eq. (4-9) do not agree with experimental results. Especially along the most leeward generator of $\phi = 180^\circ$, the small cross flow approximation theory gives a different trend from experimental distributions. For the case of $\alpha = 10^\circ$ where a separation occurs only in the very small region as shown by an oil flow visualization, eq. (4-9) gives much larger values than the experimental data. At a higher angle of attack, the calculated values are also larger than the experimental values in an unseparated region, while in a separated region the experimental values increase remarkably and the predicted values by eq. (4-9) become much smaller on the contrary; at $\alpha = 20^\circ$, the calculated value becomes one-fifth of the experimental values at its worst.

Of course, this discrepancy is due to the small cross flow approximation and the remarkable heat transfer increase along the most leeward generator must be explained by a fully three-dimensional analysis.

The good agreement with eq. (4-9) in the region of $\phi < 120^\circ$ has proved the applicability of the local similarity along the each streamline as predicted by experimental observation in chapter II.

4.3. Three-Dimensional Analysis along the Most Leeward Generator

4.3.1. Similar Transformation

The boundary layer equations along the most leeward generator are characterized by the symmetry conditions of $v=0$ and $\partial p/\partial y = \partial H/\partial y = \partial u/\partial y = \partial w/\partial y = 0$, where y denotes x_2 coordinate along the most leeward generator. Though a cross flow velocity v itself is zero on $y=0$, its lateral derivative $\partial v/\partial y$ is finite as shown by

$$\left(\frac{\partial v}{\partial y}\right)_{y=0} \sim \frac{v(\Delta y) - v(-\Delta y)}{2\Delta y} = \frac{v(\Delta y)}{\Delta y}$$

since $v(-\Delta y) = -v(\Delta y)$, where a cross flow velocity at $y = \Delta y$, $v(\Delta y)$, is finite as seen in an oil flow visualization and then $v(\Delta y)/\Delta y$ becomes large especially in a separated region. Therefore, the term $\partial v/\partial y$ plays an important role in a three-dimensional analysis along $y=0$, and the neglect of this term in the small cross flow approximation method violates the continuity equation severely which should cause a considerable effect on heat transfer calculation.

Applying symmetry conditions, basic equations (4-1)–(4-4) become

$$\frac{\partial}{\partial x}(h_2 \rho u) + \rho \frac{\partial v}{\partial y} + \frac{\partial}{\partial x_3}(h_2 \rho w) = 0 \quad (4.16)$$

$$\rho u \frac{\partial u}{\partial x} + \rho w \frac{\partial u}{\partial x_3} = -\frac{\partial p}{\partial x} + \frac{\partial}{\partial x_3} \left(\mu \frac{\partial u}{\partial x_3} \right) \quad (4.17)$$

$$\rho u \frac{\partial}{\partial x} \left(\frac{\partial v}{\partial y} \right) + \rho w \frac{\partial}{\partial x_3} \left(\frac{\partial v}{\partial y} \right) = -\frac{1}{h_2} \frac{\partial^2 p}{\partial y^2} + \frac{\partial}{\partial x_3} \left(\mu \frac{\partial}{\partial x_3} \frac{\partial v}{\partial y} \right) - \frac{\rho}{h_2} \frac{\partial v}{\partial y} \left(u \frac{\partial h_2}{\partial x} + \frac{\partial v}{\partial y} \right) \quad (4.18)$$

$$\rho u \frac{\partial H}{\partial x} + \rho w \frac{\partial H}{\partial x_3} = \frac{\partial}{\partial x_3} \left\{ \left(1 - \frac{1}{Pr} \right) \mu u \frac{\partial u}{\partial x_3} + \frac{\mu}{Pr} \frac{\partial H}{\partial x_3} \right\} \quad (4.19)$$

where eq. (4-18) was introduced by differentiating x -Momentum eq. (4-3) with respect to y , since all terms in eq. (4-3) become zero

on $y=0$. As v is the normal component to the inviscid streamline at the boundary layer edge, v at the boundary layer edge is always zero and then also $\partial v/\partial y$ is zero at the edge. Therefore, the boundary conditions for these equations are

$$\eta=0; u=v=w=\partial v/\partial y=0, H=c_p T_w$$

$$\eta \rightarrow \infty; u=u_e, v=\partial v/\partial y=0, H=c_p T_e + \frac{1}{2} u_e^2$$

Hence, the governing equations (4-16)–(4-19) are solved independently of the boundary layer solutions outside of this most leeward generator where the informations of the outside field are taken into only from the inviscid flow condition of $\partial^2 p/\partial y^2$.

Now, eqs. (4-16)–(4-19) are transformed by Lees—Levy's parabolic type similar transformation equation modified by streamline coordinate system. The parabolic type transformation was suggested by the results of Fanelop¹⁹⁾ and Lin and Rubin²⁰⁾ as mentioned in chapter I.

The transformation equations are

$$\left. \begin{aligned} \xi &= \int (\rho_w \mu_w u_e h_2^2) dx \\ \eta &= \frac{u_e h_2}{\sqrt{2\xi}} \int \rho dx_3 \end{aligned} \right\} \quad (4.20)$$

The continuity equation (4-16) is automatically satisfied by introducing a function ψ which is defined as

$$\left. \begin{aligned} h_2 \rho u &= \frac{\partial \psi}{\partial x_3} \\ h_2 \rho w + \int \rho \frac{\partial v}{\partial y} dx_3 &= -\frac{\partial \psi}{\partial x} \end{aligned} \right\} \quad (4.21)$$

Integrate the first equation of eq. (4-21) and $\psi = \sqrt{2\xi} \int u/u_e d\eta = \sqrt{2\xi} f$ is obtained where

$\frac{\partial f}{\partial \eta} = \frac{u}{u_e}$. Then the second equation provides the form for w . Now, equations (4.16)–(4.19) are transformed as

$$\begin{aligned} (Cf_{\eta\eta})_\eta + (f + \beta_3 Q)f_{\eta\eta} + \hat{\beta}_1(g - f_\eta^2) \\ = 2\xi(f_\eta f_{\eta\xi} - f_\xi f_{\eta\eta}) \end{aligned} \quad (4.22)$$

$$\begin{aligned} (CQ_{\eta\eta})_\eta + (f + \beta_3 Q)Q_{\eta\eta} - \hat{\beta}_2(g - f_\eta^2) \\ - (\beta_1 + \beta_4)f_\eta Q_\eta - \beta_3 Q_\eta^2 = 2\xi(f_\eta Q_{\eta\xi} - f_\xi Q_{\eta\eta}) \end{aligned} \quad (4.23)$$

$$\begin{aligned} (\hat{C}g_\eta)_\eta + (f + \beta_3 Q)g_\eta + (1 - G_e)\{2\hat{C}(Pr - 1)f_\eta f_{\eta\eta}\}_\eta \\ = 2\xi(f_\eta g_\xi - f_\xi g_\eta) \end{aligned} \quad (4.24)$$

where $Q_\eta \equiv \frac{1}{u_e} \frac{\partial v}{\partial y}$, $g \equiv \frac{H}{H_e}$ and subscripts η and ξ mean their partial derivatives.

Boundary layer edge parameters are defined as

$$\begin{aligned}\beta_1 &= \frac{2\xi}{u_e} \cdot \frac{\partial u_e}{\partial \xi}, & \beta_2 &= \beta_3 \cdot \frac{1}{\rho_e u_e^2} \cdot \frac{\partial^2 p}{\partial y^2} \\ \beta_3 &= \frac{2\xi}{h_2} \cdot \frac{1}{(\partial \xi / \partial x)}, & \beta_4 &= \beta_3 \cdot \frac{\partial h_2}{\partial x} \\ G_e &= \frac{h_e}{H_e}, & \hat{\beta}_1 &= \frac{\beta_1}{G_e}, & \hat{\beta}_2 &= \frac{\beta_2}{G_e}\end{aligned}\quad (4.25)$$

Boundary conditions are

$$\left. \begin{aligned} \eta &= 0; & f &= f_\eta = Q = Q_\eta = 0, & g &= g_w \\ \eta &\rightarrow \infty; & f_\eta &= g = 1, & Q_\eta &= 0 \end{aligned} \right\} \quad (4.26)$$

In the boundary layer edge parameters defined in eq. (4-25), β_2 includes the most important physical property which relates the cross flow to heat transfer as seen in eq. (4-23). Since β_2 is proportional to the curvature of a surface pressure profile in y direction at $y=0$, there are relations as

$$\text{pressure bottom at } y=0: \frac{\partial^2 p}{\partial y^2} > 0: \beta_2 > 0$$

$$\text{pressure peak at } y=0: \frac{\partial^2 p}{\partial y^2} < 0: \beta_2 < 0$$

As mentioned previously, this parameter, β_2 , brings the information outside of the symmetry plane into the solutions.

The heat transfer is expressed in the transformed coordinate as

$$\dot{q}_w = k_w \left(\frac{\partial T}{\partial x_3} \right)_w = \frac{\rho_w \mu_w u_e h_2}{Pr \sqrt{2\xi}} H_e \left(\frac{\partial g}{\partial \eta} \right)_w$$

At the forward stagnation point of $\xi \rightarrow 0$, the flow is axisymmetric and \dot{q}_w is given by Lees⁽⁴⁰⁾ as

$$\dot{q}_{wst} = \frac{1}{Pr} \sqrt{2\rho_w \mu_w} \left(\frac{du_e}{dx} \right)_{st} \cdot H_{est} \left(\frac{\partial g}{\partial \eta} \right)_{wst}$$

Therefore, the normalized heat transfer by a stagnation value is written by

$$\frac{\dot{q}_w}{\dot{q}_{wst}} = \frac{\left(\frac{p}{p_{st}} \right) u_e h_2 \sqrt{Rn}}{2 \sqrt{\left(\frac{du_e}{dx} \right)_{st} \int \left(\frac{p}{p_{st}} \right) u_e h_2^3 dx}} \left(\frac{g_{\eta w}}{g_{\eta wst}} \right) \quad (4.27)$$

where a linear viscosity law was assumed and an entropy swallowing effect was neglected. In order to obtain \dot{q}_w/\dot{q}_{wst} along $y=0$, eqs. (4-22)–(4-24) are to be solved to give $g_{\eta w}$ distribution for the given boundary layer edge parameters along $y=0$ from inviscid flow solutions.

4.3.2. Energy Integral Equation

Integrating the energy equation (4-24) with respect to η from $\eta=0$ to $\eta \rightarrow \infty$, heat transfer can be expressed after some arithmetic manipulations as

$$\dot{q}_w \propto (\hat{C}g_\eta)_w = \sqrt{2\xi} \frac{d}{d\xi} (\sqrt{2\xi} \theta_f) + \beta_3 \theta_Q \quad (4.28)$$

by using boundary conditions of $f(0)=f_\eta(0)=Q(0)=Q_\eta(0)=0$, $f_\eta(\infty)=g(\infty)=1$, and $Q_\eta(\infty)=0$. In eq. (4.28), θ_f is an usual streamwise energy thickness in two-dimensions and θ_Q is a new concept of a cross flow energy thickness defined as

$$\left. \begin{aligned} \theta_f &= \int f_\eta (1-g) d\eta \\ \theta_Q &= \int Q_\eta (1-g) d\eta \end{aligned} \right\} \quad (4.29)$$

In this definition, Q_η is proportional to v at $y=dy$ which is negative in an unseparated region. In the separated region, the cross flow velocity is reverse which means the positive $v(dy)$. This cross flow reversal is caused by the inviscid flow conditions which are conducted from the boundary layer edge to the wall and, hence, if $v(dy)$ becomes positive near the wall, the cross flow reversal should dominate across the boundary layer. Therefore, the cross flow energy thickness term $\beta_3 \theta_Q$ in eq. (4-28) becomes positive in the separated region which is generally negative in an unseparated region.

Combining θ_f and θ_Q , the three-dimensional energy thickness along $y=0$ can be defined as

$$\theta = \int \frac{\rho u}{\rho_e u_e} (1-g) dx + \frac{1}{\rho_e u_e h_2} \int \rho_e u_e \frac{\partial}{\partial y} \cdot \left\{ \int \frac{\rho v}{\rho_e u_e} (1-g) dx \right\} dy$$

Then, heat transfer can be described by

$$\dot{q}_w \propto (\hat{C}g_\eta)_w = \sqrt{2\xi} \frac{d}{d\xi} (h_2 \rho_e u_e \theta)$$

which is the same form for a two-dimensional flow as given by Beckwith⁽⁵⁰⁾.

If the local similarity is assumed, eq. (4-28) becomes

$$(\hat{C}g_\eta)_w = \theta_f + \beta_3 \theta_Q \quad (4.30)$$

If the small cross flow together with the local similarity is assumed, eq. (4-28) is

$$(\hat{C}g_\eta)_w = \theta_f \quad (4.31)$$

Therefore, the cross flow term $\beta_3 \theta_Q$ is considered as a correction term for the value given by the small cross flow approximation method.

Now, in order to investigate the cross flow effect on heat transfer, the behavior of the cross flow energy thickness term $\beta_3 \theta_Q$ is observed qualitatively. For this purpose, eqs. (4-22)–(4-24) were solved numerically with the local similarity assumption as described in detail in the subsequent section. This similar

solutions provide significant relations of

$$\left. \begin{array}{l} Q_\eta < 0 \text{ and } v(\Delta y) < 0 \text{ if } \beta_2 > 0 \\ Q_\eta > 0 \text{ and } v(\Delta y) > 0 \text{ if } \beta_2 < 0 \end{array} \right\} \quad (4.32)$$

throughout a boundary layer as shown in Fig. 13 where examples of boundary layer profiles of f_η , Q_η , and g are presented. This relation shows that once a pressure peak appears at $y=0$ in a pressure profile in y direction, in other words, once flow experiences an adverse pressure gradient near $y=0$, the cross flow velocity component becomes reverse which resulted in a cross flow separation.

From the definition of θ_Q ,

$$\begin{aligned} \theta_Q &= \int Q_\eta (1-g) d\eta = \int \frac{1}{u_e} \frac{\partial v}{\partial y} (1-g) d\eta \\ &= \int \frac{v(\Delta y)}{u_e \Delta y} (1-g) d\eta \end{aligned}$$

where $1-g \geq 0$ for $\eta=0 \sim \infty$. Therefore, from the relation (4-32), the cross flow energy thickness term has the relation of

$$\left. \begin{array}{l} \beta_3 \theta_Q \leq 0 \text{ if } \beta_2 \geq 0 \\ \beta_3 \theta_Q > 0 \text{ if } \beta_2 < 0 \end{array} \right\} \quad (4.33)$$

Consequently, it can be said qualitatively that in an unseparated upstream region, the cross flow correction term is negative and then heat transfer becomes smaller than the value given by small cross flow approximation method, but that in a separated downstream region, the correction term is positive and hence heat transfer becomes larger than the value by the small cross flow theory. This features agree with the experimental heat transfer distribution as seen in Fig. 7.

The physical explanation for this heat transfer increase in a separated region can be provided by the discussions of the three-dimensional displacement thickness of the boundary layer along $y=0$. Applying the equivalent source method presented by Lighthill⁵²⁾ in general three-dimensional flow, the three-dimensional displacement thickness of a compressible boundary layer along $y=0$ can be obtained as follows; the out flow at the boundary layer edge is given by integrating continuity equation (4-16) as

$$\begin{aligned} h_2 \rho_e w_e &= -\frac{\partial}{\partial x} (h_2 \rho_e u_e x_3) \\ &+ \frac{\partial}{\partial x} \left\{ h_2 \rho_e u_e \int \left(1 - \frac{\rho u}{\rho_e u_e} \right) dx_3 \right. \\ &\left. - \iint \rho \frac{\partial v}{\partial y} dx dx_3 \right\} \end{aligned} \quad (4.34)$$

where the first term in the right hand side is the out flow existing in a curved inviscid flow,

while the second term is an additional out flow caused by the boundary layer displacement. Now, the effect of the boundary layer on the external inviscid flow is replaced by a source distribution on the surface between streamlines of $y=0$ and $y=\Delta y$. The source strength m is given by eq. (4-34) as

$$m = \frac{1}{h_2} \frac{\partial}{\partial x} \left[h_2 \rho_e u_e \int \left(1 - \frac{\rho u}{\rho_e u_e} \right) dx_3 - \iint \rho \frac{\partial v}{\partial y} dx dx_3 \right]$$

The new fluid emitted from the sources is assumed to fill the cross section with the area of $\delta^* h_2 \Delta y$ by the mass flow rate of $\rho_e u_e$. Since the total mass emitted in $x=0 \sim x$ should pass $\delta^* h_2 \Delta y$, then

$$\int m h_2 \Delta y dx = \rho_e u_e \delta^* h_2 \Delta y$$

Therefore, the three-dimensional displacement thickness of the compressible boundary layer along $y=0$ can be described as

$$\delta^* = \delta_f^* + \delta_Q^* \quad (4.35)$$

where

$$\begin{aligned} \delta_f^* &= \frac{\sqrt{2\xi}}{\rho_e u_e h_2} \int \left(\frac{\rho_e}{\rho} - f_\eta \right) d\eta \\ \delta_Q^* &= -\frac{1}{\rho_e u_e h_2} \int \frac{\sqrt{2\xi}}{h_2 \xi_x} \int Q_\eta d\eta d\xi \end{aligned}$$

δ_Q^* is named a cross flow displacement thickness and is considered as the cross flow correction term for the displacement thickness given by the small cross flow approximation theory.

From the relation (4-32), the cross flow displacement thickness has the relation of

$$\left. \begin{array}{l} \delta_Q^* > 0 \text{ if } \beta_2 > 0 \\ \delta_Q^* < 0 \text{ in the region of } \beta_2 < 0 \end{array} \right\} \quad (4.36)$$

Concluding from these qualitative investigations, the heat transfer increase along the most leeward generator in a separated region can be explained physically as follows; in an upstream region without separation, fluid in a boundary layer is forced to flow toward the symmetric plane as a cross flow by a favorable pressure gradient and the piling up of mass flow at $y=0$ makes the displacement thickness thicker and hence heat transfer becomes small. However, when fluid experiences an adverse pressure gradient in a downstream region corresponding to a large cross flow Mach number gradient from supersonic to subsonic in a shock layer, the cross flow velocity component in a boundary layer becomes reverse and the

reverse cross flow in the resulted separated region makes the displacement thickness thinner and hence heat transfer becomes large.

Although the heat transfer increase along the symmetric plane has been explained by the cross flow reversal in this section, this phenomena also may be recognized as the reattachment of the separated flow. However, in the present cases, the reattachment may be so weak that the impinging effect of the separated shear flow may be negligible which should induce a strong interaction with the external inviscid flow.

The analysis along the symmetric plane provides the cross flow reversal for the negative β_2 , but it does not immediately mean the occurrence of the recirculating flow of the free vortex layer type, though the reverse cross flow should always occur in the separated flow region. In order to obtain the exact condition for the occurrence of the separated flow, the investigation of the fully three-dimensional flow over the lee-surface should be required.

4.3.3. Locally Similar Solution along $y=0$

The three-dimensional boundary layer equations along the most leeward generator have been solved numerically with the assumption of local similarity. The similar forms of eqs. (4-22)–(4-24) are

$$f_{\eta\eta\eta} + (f + \beta_3 Q) f_{\eta\eta} + \beta_1 (g - f_{\eta}^2) = 0 \quad (4.37)$$

$$Q_{\eta\eta\eta} + (f + \beta_3 Q) Q_{\eta\eta} - \beta_2 (g - f_{\eta}^2) - (\beta_1 + \beta_4) f_{\eta} Q_{\eta} - \beta_3 Q_{\eta}^2 = 0 \quad (4.38)$$

$$g_{\eta\eta} + Pr(f + \beta_3 Q) g_{\eta} + 2(1 - G_e)(Pr - 1) \cdot (f_{\eta} f_{\eta\eta})_{\eta} = 0 \quad (4.39)$$

where Rubesin constant C is assumed to be unity and Pr is assumed constant.

Eqs. (4-37)–(4-39) are solved numerically by the quasi-linearization method as described briefly here. This is an extension of the method employed in two-dimensional cases by Werle⁶⁴⁾ and Inouye et al.⁶⁵⁾

The true solutions of f, Q, g are expressed by trial solutions of $\tilde{f}, \tilde{Q}, \tilde{g}$ and error terms $\Delta f, \Delta Q, \Delta g$ as

$$f = \tilde{f} + \Delta f$$

$$Q = \tilde{Q} + \Delta Q$$

$$g = \tilde{g} + \Delta g$$

Substituting these into eqs. (4-37)–(4-39) and neglecting quadratic error terms, equations are linearized as

$$F1_{\eta\eta} + (\tilde{f} + \beta_3 \tilde{Q}) F1_{\eta} - 2\beta_1 \tilde{F}1 \cdot F1 = -\beta_1 (\tilde{g} + \tilde{F}1^2)$$

$$Q1_{\eta\eta} + (\tilde{f} + \beta_3 \tilde{Q}) Q1_{\eta} - \{(\beta_1 + \beta_4) \tilde{F}1 + 2\beta_3 \tilde{Q}1\} \cdot Q1 = \beta_2 (\tilde{g} - \tilde{F}1^2) - \beta_3 \tilde{Q}1^2$$

$$g_{\eta\eta} + Pr(\tilde{f} + \beta_3 \tilde{Q}) g_{\eta} = 2(1 - G_e) \cdot (1 - Pr) \cdot (\tilde{F}1 \cdot \tilde{F}1_{\eta})_{\eta} \quad (4.40)$$

where $F1 = f_{\eta}$, $Q1 = Q_{\eta}$ and then f and Q can be obtained by $f = \int F1 d\eta$ and $Q = \int Q1 d\eta$.

Boundary conditions are

$$\begin{aligned} \eta=0: & F1=Q1=0, \quad g=g_w \\ \eta \rightarrow \infty: & F1=g=1, \quad Q1=0 \end{aligned} \quad (4.41)$$

If 1st and 2nd derivatives in eq. (4-40) are approximated by 2nd order central difference as

$$F1_{\eta} = \frac{F1_{i+1} - F1_{i-1}}{2\Delta\eta}, \quad F1_{\eta\eta} = \frac{F1_{i+1} - 2F1_i + F1_{i-1}}{\Delta\eta^2},$$

eq. (4.40) can be written as

$$\begin{aligned} [AF^n] \quad \vec{F}1^{n+1} &= \vec{D}\vec{F}^n \\ [AQ^n] \quad \vec{Q}1^{n+1} &= \vec{D}\vec{Q}^n \\ [AG^n] \quad \vec{g}^{n+1} &= \vec{D}\vec{G}^n \end{aligned} \quad (4.42)$$

where $\vec{F}1^{n+1}$, $\vec{Q}1^{n+1}$, \vec{g}^{n+1} are row vectors with components of $F1_i^{n+1}$, $Q1_i^{n+1}$, g_i^{n+1} , $i=2 \sim N-1$ at $(n+1)$ th iteration number and coefficients matrices $[AF^n]$, $[AQ^n]$, $[AG^n]$ have tridiagonal forms as shown in APPENDIX C. Then solutions of $F1$, $Q1$, g at $(n+1)$ th iteration can be obtained from eq. (4.40) with known values of $[AF^n]$, $[AQ^n]$, $[AG^n]$, $\vec{D}\vec{F}^n$, $\vec{D}\vec{Q}^n$ and $\vec{D}\vec{G}^n$ at (n) th iteration until they become converged.

The similar solutions have been obtained for widely ranged parameters of β_1 , β_2 , β_3 , β_4 and G_e with $Pr=0.7$ and $g_w=0.38$. These ranges of parameters are covering the boundary layer edge conditions along the most leeward generator of a blunt cone at $\alpha \leq 20^\circ$ in $M_\infty=7 \sim 10$.

In Fig. 13, the similar solutions for boundary layer profiles of f_{η} , Q_{η} and g against η are presented for $\beta_1=0.0$, $0.02 \leq \beta_2 \leq -5.2$, $\beta_3=6.0$, $\beta_4=0.0$ and $G_e=0.4$. The profiles for Q_{η} show the cross flow reversal throughout the boundary layer for negative β_2 and "S" character profile does not appear for any β_2 . Fig. 14 shows solutions of $(Q_{\eta\eta w})_{y=0}$ which is proportional to a cross flow velocity gradient on the wall at $y=dy$ as

$$(Q_{\eta\eta w})_{y=0} = \frac{1}{u_e} \left(\frac{\partial}{\partial \eta} \frac{\partial v}{\partial y} \right)_{w, y=0} \sim \frac{1}{u_e \Delta y} \left(\frac{\partial v(\Delta y)}{\partial \eta} \right)_w$$

Hence, this figure shows the shear force reversal for negative β_2 , which was demonstrated by an oil flow visualization.

The solutions for $g_{\eta w}$ are shown in Fig. 15. They are correlated by following equations as functions of β_2 , β_3 , and Ge ;

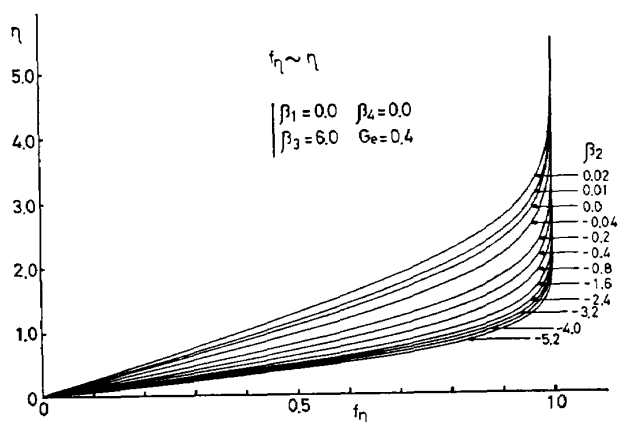


Fig. 13a. Similar Solutions for Flow Profile;
 $f_{\eta} \sim \eta$

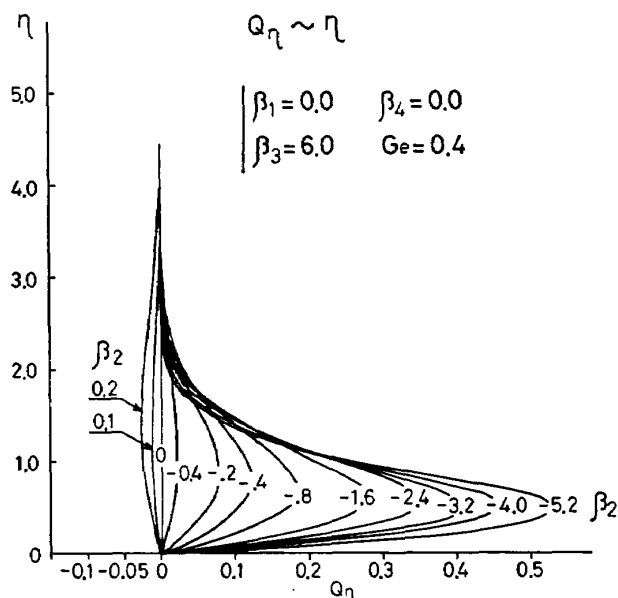


Fig. 13b. Similar Solutions for Flow Profile;
 $Q_{\eta} \sim \eta$

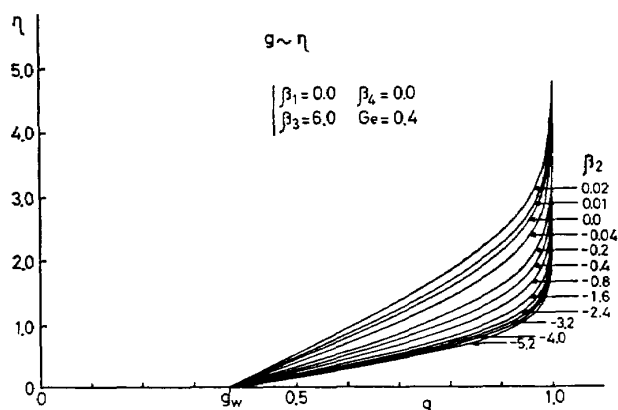


Fig. 13c. Similar Solutions for Flow Profile;
 $g \sim \eta$

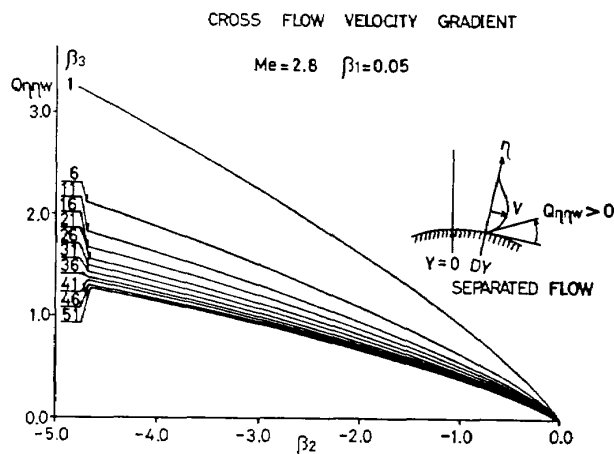


Fig. 14. Cross Flow Velocity Gradient on Wall

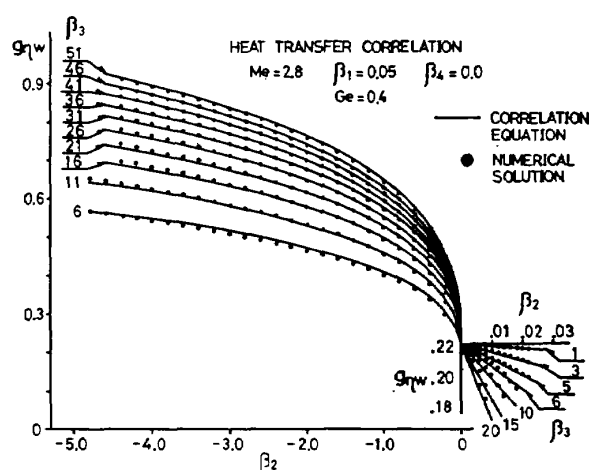


Fig. 15. Enthalpy Gradient on Wall

$$\left. \begin{aligned} g_{\eta w} &= \frac{1}{B} - \left(E - \frac{1}{B}\right) \frac{1}{D} \beta_2 & \text{for } \beta_2 > 0 \\ g_{\eta w} &= \left(\frac{1+A|\beta_2|^N}{B+C|\beta_2|^N} \right) & \text{for } \beta_2 \leq 0 \end{aligned} \right\} \quad (4.43)$$

where

$$E = \frac{1+A|D|^N}{B+C|D|^N}$$

$$N = \frac{1}{\beta_3 + 1.4} + 0.445$$

$$B = -1.41Ge + 5.04$$

$$C = -Ge + 1.8$$

$$D = \left(\frac{0.153}{\beta_2 + 2.44} \right) - 2.8 \times 10^{-4}$$

$$A = \left(\frac{1 + a\beta_3^n}{2 + c\beta_3^n} \right)$$

$$a = -2.4(Ge - 0.75)$$

$$c = -0.085(Ge - 1.56)$$

$$n = 0.353(Ge + 1.124)$$

This correlation equation is fitted in solutions

within 5% accuracy for the following ranges of parameters;

$$\begin{aligned} |\beta_1| < 0.05, \quad |\beta_4| < 1.0, \quad 0.3 < G_e < 0.4 \\ 5 < \beta_3 < 100 \quad \text{for} \quad -5.0 < \beta_2 \leq 0.0 \quad \text{and} \\ 1 < \beta_3 < 25 \quad \text{for} \quad 0.0 \leq \beta_2 < 0.03 \end{aligned}$$

The effects of β_1 and β_4 on g_{7w} are small within the above ranges and neglected in this correlation equation. The above applicable ranges of parameters cover the conditions along the most leeward generator of a blunt cone at $\alpha \leq 20^\circ$ and this shows a narrow range of the streamwise pressure gradient β_1 which has important role in two-dimensional separation.

As seen in Fig. 15, when β_1 decreases to negative value, heat transfer increases remarkably. The behavior of the cross flow energy thickness term of $\beta_3 \theta_Q$ is presented in Fig. 16.

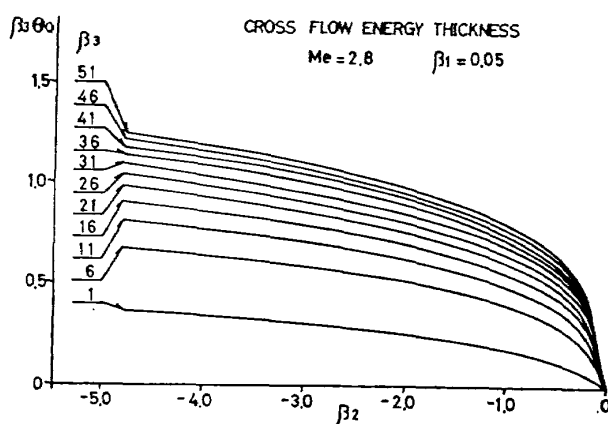


Fig. 16. Cross Flow Energy Thickness

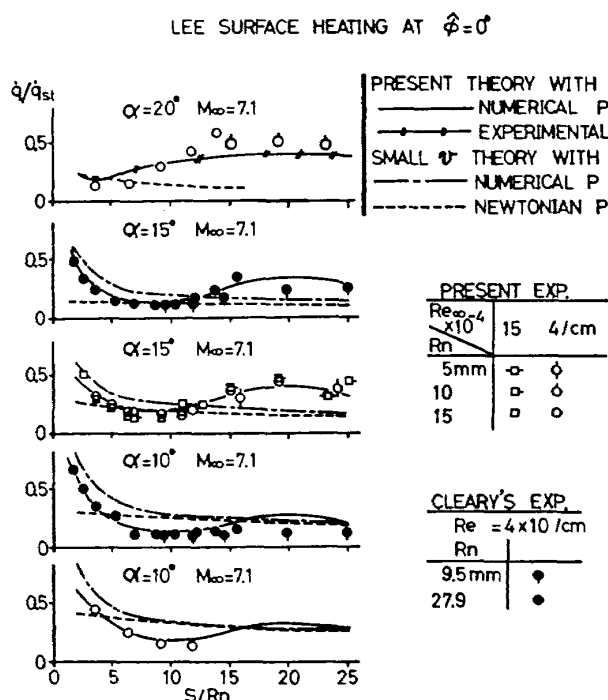


Fig. 17. Most Leeward Heat Transfer Distribution

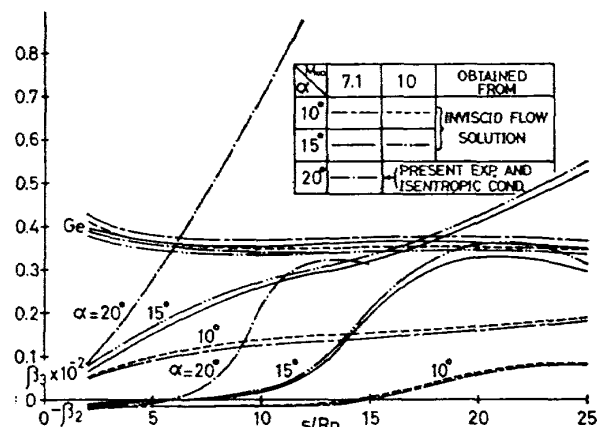


Fig. 18. Boundary Layer Edge Parameters along $y=0$

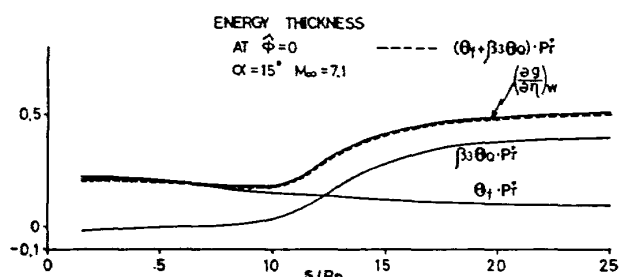


Fig. 19. Energy Thickness along $y=0$

The correlation equation (4-43) has been applied to a blunt cone at angles of attack $\alpha = 10^\circ, 15^\circ, 20^\circ$ at $M_\infty = 7.1$ and 10. The heat transfer distribution along the most leeward generator are obtained as shown in Fig. 17 compared with experimental data. Also shown in the same figure are the results calculated by the small cross flow theory using the pressure distribution given both by inviscid flow solutions and by Newtonian theory. As seen in this figure, the present cross flow theory can provide good agreement with experimental data. The boundary layer edge parameters for these cases are presented in Fig. 18 along $y=0$. The energy thickness is obtained by integrating the similar solutions for the corresponding boundary layer edge parameters at each locations along $y=0$. Fig. 19 shows the remarkable increase of cross flow energy thickness term $\beta_3 \theta_Q$ and the summation of θ_f and $\beta_3 \theta_Q$ is shown to satisfy eq. (4-30).

These quantitative investigations comparing with experimental data have proved the validity of the qualitative discussions in the previous section.

On the way of solving similar boundary layer equations on the symmetry plane, numerical difficulties were encountered for the large β_2 ,

while no difficulty was encountered for small β_2 and for all negative β_2 . Comparing with the results for a sharp cone by Moore⁴¹⁾ and Lin and Rubin²⁰⁾, a large β_2 corresponds to a large α without separation where Moore could not obtain a solution and Lin and Rubin obtained a thick nonsimilar boundary layer. A negative β_2 corresponds to a large α with separation where Lin and Rubin suggested a similar boundary layer along $y=0$. For the present calculation on the most leeward generator over a blunt cone, the large β_2 has not occurred and the results show the good applicability of a similar boundary layer approximation for heat transfer on the leeward symmetric plane.

Concluding from these investigations, the present cross flow theory based on the local similarity assumption can be said to provide the reasonable results for heat transfer along the most leeward generator at the moderate angle of attack.

V. CONCLUSIONS

The theoretical and experimental investigations about heat transfer over a blunt cone at angles of attack in hypersonic flow have been conducted and the following concluding remarks have been drawn;

(1) A cross flow separation can occur even on a lee-surface with a positive local angle of attack so long as a boundary layer experiences an adverse pressure gradient in the direction "p" normal to the trough of isobaric lines on the surface.

(2) The new criterion for the three-dimensional boundary layer separation is given by

$$(\tau_p)_w = \left(\mu \frac{\partial V_p}{\partial x_3} \right)_w = 0$$

(3) The boundary layer thickness in the separated region is proved theoretically and experimentally not so thick as to affect the inviscid flow properties significantly.

(4) The new definitions of cross flow energy thickness and cross flow displacement thickness provide a physical explanation for the remarkable heat transfer increase along the most leeward generator in a separated boundary layer.

(5) The validity of the assumption of the local similarity has been proved experimentally and numerically.

(6) The locally similar solutions of the three-dimensional boundary layer equations show an immediate cross flow reversal after the appearance of an adverse pressure gradient in "p" direction, although the experiments

exhibited a little after the appearance of it.

(7) The remarkable heat transfer increase along the most leeward generator is well predicted by the present cross flow theory.

(8) The small cross flow approximation method is shown to be satisfactory in the region where the small secondary flow in the boundary layer has been predicted by comparing the inviscid flow solutions and oil flow visualization.

ACKNOWLEDGEMENTS

The author would like to express his sincere gratitude to Professor Y. Aihara of University of Tokyo for his valuable advices and encouragement during the course of the present study.

The author would like to acknowledge the helpful discussions of Dr. I. Wada, head of 1st Aerodynamics Division. He is also grateful to the staff of Hypersonic Wind Tunnel Facilities and Instrumentation Sections for their vigorous works with the excellent technique for operations and measurements through the present experimental investigations.

REFERENCES

- 1) Cooke, J. C., Hall, M. G., "Boundary Layer in Three Dimensions," Progress in Aeronautical Science, Vol. II. "Boundary Layer Problems" edited by D. Kuchemann and A. Ferri, Pergamon Press, New York 1962, pp. 221-285.
- 2) Mager, A., "Three-Dimensional Laminar Boundary Layers," High Speed Aerodynamics and Jet Propulsion: Theory of Laminar Flow, edited by F. K. Moore, Vol. IV, Princeton University Press, New Jersey, 1964, pp. 284-394.
- 3) Crabtree, L. F., Kuchemann, D., Sowerby, L., "Three-Dimensional Boundary Layers," Laminar Boundary Layers, edited by L. Rosenhead, Oxford University Press, 1963, pp. 409-491.
- 4) Korkegi, R. H., "Survey of Viscous Interactions Associated with High Mach Number Flight," AIAA J. Vol. 9, No. 5, May 1971.
- 5) Hefner, J. N., Whitehead, A. H. Jr., "Experimental Lee-Surface Heating Studies on a Delta-Wing Orbiter," NASA TM X-2272, 1971.
- 6) Maise, G., "Lee-Surface Heating Investigations of Simple Body-Like Configurations," NASA TM X-2272, 1971.
- 7) Hefner, J. N., Whitehead, A. H. Jr., "Studies of Lee-Surface Heating at Hy-

- personic Mach Numbers," NASA TM X-2570, 1972.
- 8) Whitehead, A. H. Jr., Keys, J. W., "Flow Phenomena and Separation over Delta Wings with Trailing-Edge Flaps at Mach 6," AIAA J. Vol. 6, No. 12, Dec. 1968.
 - 9) Cleary, J. W., "An Experimental and Theoretical Investigation of Pressure Distribution and Flow Fields of Blunt Cones at Hypersonic Mach Number," NASA TN D-2969, 1965.
 - 10) Cleary, J. W., "Effects of Angle of Attack and Bluntness on Laminar Heating-Rate Distribution of a 15 Cone at Mach Number of 10.6," NASA TN D-5450, 1969.
 - 11) Rao, D. M., "Hypersonic Lee-Surface Heating Alleviation on Delta Wing by Apex-Drooping," AIAA J. Vol. 9, No. 9, Sept. 1971.
 - 12) Peake, D. J., Rainbird, W. J., Atraghji, E. G., "Three Dimensional Flow Separations on Aircraft and Missiles," AIAA J. Vol. 10, No. 5, May 1972.
 - 13) Zakkay, V., Miyazawa, M., Wang, C. R., "Lee-Surface Flow Phenomena over Space Shuttle at Large Angle of Attack at $M=6$," AIAA Paper 75-148, 1975.
 - 14) Zakkay, V., Economos, C., Alzner, E., "Leeside Flow Field Description over Cones at Large Incidence," AFFDL-TR-74-19, Advanced Tech. Lab., July 1974.
 - 15) Nomura, S., Hashimoto, H., Yoshizawa, A., Hozumi, K., "The Viscous Flow over Axisymmetric Body with and without Angle of Attack at $M=7$," Proceedings of 10th ISTS, AGNE Publishing Inc., Tokyo, 1973.
 - 16) DeJarnette, F. R., Hamilt, H. H., "Inviscid Surface Streamlines and Heat Transfer on Shuttle Type Configurations," J. Spacecraft, Vol. 10, No. 5, May 1973.
 - 17) DeJarnette, F. R., Davis, R. M., "A Simplified Method for Calculating Laminar Heat Transfer over Bodies at an Angle of Attack," NASA TN D-4720, 1968.
 - 18) Der, J. Jr., "A Study of General Three-Dimensional Boundary-Layer Problems by an Exact Numerical Method," AIAA J. Vol. 9, No. 7, July 1971.
 - 19) Fannelop, T. K., "A Method of Solving the Three-Dimensional Laminar Boundary Layer Equations with Application to a Lifting Re-Entry Body," AIAA J. Vol. 6, No. 6, June 1968.
 - 20) Lin, T. C., Rubin, S. G., "Viscous Flow over a Cone at Moderate Incidence," Part 2, Supersonic Boundary Layer, J. Fluid Mech., Vol. 59, Part 3, 1973.
 - 21) Lubard, S. C., Helliwell, W. S., "Calculation of the Flow on a Cone at High Angle of Attack," AIAA J. Vol. 12, No. 7, July 1974.
 - 22) Nomura, S., "Lee-Surface Heating of Blunt Cone at Angle of Attack," Proceedings of 11th ISTS, AGNE Publishing Inc., Tokyo, 1975.
 - 23) Lubard, S. C., Rakich, J. V., "Calculation of the Flow on a Blunt Cone at a High Angle of Attack," AIAA Paper No. 75-149, 1975.
 - 24) McRae, D. S., "A Numerical Study of Supersonic Viscous Cone Flow at High Angle of Attack," AIAA Paper No. 76-97, 1976.
 - 25) Nomura, S., "Similar Boundary Layer Analysis for Lee-Surface Heating on Yawed Blunted Cone," AIAA Paper No. 76-122, 1976; also in the same title, AIAA J. Vol. 14, No. 14, Nov. 1976.
 - 26) Wang, K. C., "Separation Patterns of Boundary Layer over an Inclined Body of AIAA J. Vol. 14, No. 14, Nov. 1976.
 - 27) Wang, K. C., "Three-Dimensional Boundary Layer near the Plane of Symmetry of a Spheroid at Incidence," J. Fluid Mech. Vol. 43, Part 1, 1970.
 - 28) Maskell, E. C., "Flow Separation in Three Dimensions," RAE Rept. Aero 2565, Nov. 1955.
 - 29) Moretti, G., Bleich, B., "Three-Dimensional Flow around Blunt Bodies," AIAA J. Vol. 5, No. 9, Sept. 1967.
 - 30) Barnwell, R. W., "A Time-Dependent Method for Calculating Supersonic Angle-of-Attack Flow about Axisymmetric Blunt Bodies with Sharp Shoulders and Smooth Nonaxisymmetric Blunt Bodies," NASA TN D-6283, 1971.
 - 31) MacCormack, R. W., "The Effect of Viscosity in Hypersonic Impact Cratering," AIAA Paper 69-354, 1969.
 - 32) Thomas, P. D., Vinokura, M., Bstianon, A., Conti, R. J., "Numerical Solution for Three-Dimensional Inviscid Supersonic Flow," AIAA J. Vol. 10, No. 7, July 1972.
 - 33) Kutler, P., Warming, R. F., Lomax, H., "Computation of Space Shuttle Flow Field Using Noncentered Finite-Difference Schemes," AIAA J. Vol. 11, No. 2, Feb. 1973.
 - 34) Moretti, G., Grossman, B., Marconi, Jr., F., "A Complete Numerical Technique for the Calculation of Three-Dimensional In-

- viscid Supersonic Flows," AIAA Paper No. 72-192, 1972.
- 35) Tracy, R. R., "Hypersonic Flow over a Yawed Circular Cone," Hypersonic Research Project, GALCIT Memo. No. 69, Aug. 1963.
 - 36) Whitehead, A. H., Jr., "Effect of Vortices on Delta Wing Lee-Side Heating at Mach 6," AIAA J. Vol. 8, No. 3, March 1970.
 - 37) Whitehead, A. H., Jr., Bertram, M. H., "Alleviation of Vortex-Induced Heating to the Lee Side of Slender Wings in Hypersonic Flow," AIAA J. Vol. 9, No. 9, Sept. 1971.
 - 38) Stetson, K. F., "Boundary Layer Separation on Slender Cone at Angle of Attack," AIAA J. Vol. 10, No. 5, May 1972.
 - 39) Rao, D. M., Whitehead, A. H. Jr., "Lee-Side Vortices on Delta Wings at Hypersonic Speeds," AIAA J. Vol. 10, No. 11, No. 1972.
 - 40) Vaglio-Laurin, R., "Laminar Heat Transfer on Three-Dimensional Blunt-Nosed Bodies in Hypersonic Flow," Jet Propulsion, Vol. 29, No. 2, Feb. 1959.
 - 41) Moore, F. K., "Three-Dimensional Laminar Boundary-Layer Flow," J. Aeron. Sci. Vol. 20, Aug. 1953.
 - 42) VanDyke, M. D., "The Supersonic Blunt-Body Problem-Review and Extension," J. Aerospace Sci., Vol. 25, No. 8, Aug. 1958.
 - 43) Inouye, M., Rakich, J. V., Lomax, H., "A Description of Numerical Methods and Computation Programs for Two-Dimensional and Axisymmetric Supersonic Flow over Blunt-Nosed and Flared Bodies," NASA TN D-2970, 1965.
 - 44) Ferri, A., "The Method of Characteristics," General Theory of High Speed Aerodynamics, Princeton Univ. Press, New Jersey, 1954, pp. 583-747.
 - 45) Babenko, K. I., Voskresenski, G. P., Lyubimov, A. N., Rusanov, V. V., "Three-Dimensional Flow of Ideal Gas Past Smooth Bodies," NASA TT F-380, 1966.
 - 46) Moretti, G., "Importance of Boundary Conditions in the Numerical Treatment of Hyperbolic Equations," Physics of Fluids, Supplement II, Vol. 12, No. 12, Part II, 1969.
 - 47) Richtmyer, R. D., Morton, K. W., Difference Methods for Initial Value Problems, Interscience Publishers, New York, 1967.
 - 48) Cleary, J. W., "Effects of Angle of Attack and Bluntness on the Shock-Layer Properties of a 15° Cone at a Mach Number 10.6," NASA TN D-4909, 1968.
 - 49) Lees, L., "Laminar Heat Transfer over Blunt-Nosed Bodies at Hypersonic Flight Speeds," Jet Propulsion, Vol. 26, No. 4, April 1956.
 - 50) Beckwith, I. E., Cohen, N. B., "Application of Similar Solution to Calculation of Laminar Heat Transfer on Bodies with Yawed and Large Pressure Gradient in High-Speed Flow," NASA TN D-625, 1961.
 - 51) Kemp, N. H., Rose, P. H., Detra, R. W., "Laminar Heat Transfer around Blunt Bodies in Dissociated Air," J. of Aeron. Science, Vol. 26, No. 7, 1959.
 - 52) Lighthill, M. J., "On Displacement Thickness," J. Fluid Mech., Vol. 4, 1958.
 - 53) Libby, P. A., Liu, T. M., "Some Similar-Laminar Flows Obtained by Quasilinearization," AIAA J. Vol. 6, No. 8, Aug. 1968.
 - 54) Werle, M. J., Bertke, S. D., "A Finite-Difference Method for Boundary Layer with Reverse Flow," AIAA J. Vol. 10, No. 9, Sept. 1972.
 - 55) Inouye, K., Tate, A., "Finite-Difference Version of Quasi-Linearization Applied to Boundary-Layer Equations," AIAA J. Vol. 12, No. 4, April 1974.
 - 56) Yoshizawa, A., Nomura, S., "A Finite-Difference Solution for Three-Dimensional Supersonic Inviscid Flow," NAL TM-316, 1976 (in Japanese).

APPENDIX A

The coefficient matrices [A] and [B] in the basic equations (3-5) of the three-dimensional inviscid flow are given by

$$[A] = [\bar{A}] \frac{\partial f}{\partial r} + [\bar{B}] \frac{\partial f}{\partial \phi} + [I] \frac{\partial f}{\partial z}$$

$$[B] = [\bar{B}] \frac{\partial g}{\partial \phi}$$

where [I] is an identity matrix and $[\bar{A}]$ and $[\bar{B}]$ are defined as

$$[\bar{A}] = r \begin{vmatrix} \rho u_1 u_3^2 & 0 & \rho^2 a^2 u_3^2 & 0 & -\rho^2 a^2 u_1 u_3 \\ \rho u_1 & \bar{\eta} \rho u_1 & \rho^2 u_3^2 & 0 & -\rho^2 u_1 u_3 \\ \bar{\eta} & 0 & \bar{\eta} \rho u_1 & 0 & 0 \\ 0 & 0 & 0 & \bar{\eta} \rho u_1 & 0 \\ -u_1 u_3 & 0 & -\rho a^2 u_3 & 0 & \rho u_1 u_3^2 \end{vmatrix}$$

$$[\bar{B}] = \begin{vmatrix} \rho u_2 u_3^2 & 0 & 0 & \rho^2 a^2 u_3^2 & -\rho^2 a^2 u_2 u_3 \\ \rho u_2 & \bar{\eta} \rho u_2 & 0 & \rho^2 u_3^2 & -\rho^2 u_2 u_3 \\ 0 & 0 & \bar{\eta} \rho u_2 & 0 & 0 \\ \bar{\eta} & 0 & 0 & \bar{\eta} \rho u_2 & 0 \\ -u_2 u_3 & 0 & 0 & -\rho a^2 u_3 & \rho u_2 u_3^2 \end{vmatrix}$$

$$\begin{aligned}
BG_i^n &= -4 \\
CG_i^n &= 2 + \Delta\eta \cdot Pr(F_i^n + \beta_3 Q_i^n) \\
DF_i^n &= -2\Delta\eta^2 \beta_1 (g_i^n + F1_i^{n2}) \\
DQ_i^n &= 2\Delta\eta^2 \{\beta_2 (g_i^n - F1_i^{n2}) - \beta_3 Q1_i^{n2}\} \\
DG_i^n &= -4\Delta\eta^2 (1 - G_e) C(Pr - 1) (F1_i^n F3_i^n + F2_i^{n2}) \\
F2_i^n &= (F1_{i+1}^n - F1_{i-1}^n) / 2\Delta\eta \\
F3_i^n &= (F2_{i+1}^n - F2_{i-1}^n) / 2\Delta\eta
\end{aligned}$$

Boundary conditions are

$$\begin{aligned}
F1_1^n &= Q1_1^n = 0 \quad \text{and} \quad g_1^n = g_w \quad \text{at} \quad i=1 \\
F1_N^n &= g_N^n = 1 \quad \text{and} \quad Q1_N^n = 0 \quad \text{at} \quad i=N
\end{aligned}$$

Then, eq. (C-1) becomes

$$\begin{vmatrix}
BF_2^n & CF_2^n & \dots & \dots & 0 \\
AF_3^n & BF_3^n & CF_3^n & & \\
\vdots & & & & \vdots \\
\vdots & & AF_{N-2}^n & BF_{N-2}^n & CF_{N-2}^n \\
0 & \dots & \dots & AF_{N-1}^n & BF_{N-1}^n
\end{vmatrix}
=
\begin{vmatrix}
F1_2^{n+1} \\
F1_3^{n+1} \\
\vdots \\
F1_{N-2}^{n+1} \\
F1_{N-1}^{n+1}
\end{vmatrix}
=
\begin{vmatrix}
DF_3^n \\
DF_3^n \\
\vdots \\
DF_{N-2}^n \\
DF_{N-1}^n CF_{N-1}^n
\end{vmatrix} \quad (C.2)$$

and in the similar form for $Q1$ and g .

For the tridiagonal equation (C-2), the recurring equation can be constructed easily as

$$F1_i = \frac{\overline{DF}_i^n}{\overline{BF}_i^n} - \left(\frac{CF_i^n}{\overline{DF}_i^n} \right) \cdot F1_{i+1}^{n+1} \quad \text{for } i=N-2 \sim 2 \quad (C-3)$$

where

$$\begin{aligned}
\overline{BF}_i^n &= BF_i^n - AF_i^n \cdot CF_{i-1}^n / \overline{BF}_{i-1}^n \\
\overline{DF}_i^n &= DF_i^n - AF_i^n \cdot \overline{DF}_{i-1}^n / \overline{BF}_{i-1}^n \\
&\quad \text{for } i=3 \sim N-2
\end{aligned}$$

with

$$\overline{BF}_2^n = BF_2^n, \quad \overline{DF}_2^n = DF_2^n$$

The similar recurring equations for $Q1$ and g can be obtained.

From these recurring formulas, eq. (C-2) can be solved easily.

TECHNICAL REPORT OF NATIONAL
AEROSPACE LABORATORY
TR-494T

航空宇宙技術研究所報告 494T 号 (欧文)

昭和 52 年 3 月 発行

発 行 所	航 空 宇 宙 技 術 研 究 所 東 京 都 調 布 市 深 大 寺 町 1,880 電 話 武 蔵 野 三 鷹 (0422)47-5911 (大 代 表)
印 刷 所	株 式 会 社 東 京 プ レ ス 東 京 都 板 橋 区 桜 川 2 丁 目 27 の 12

Published by
NATIONAL AEROSPACE LABORATORY
1,880 Jindaiji, Chōfu, Tokyo
JAPAN
